Summer 2022

Effect of boron in cast iron

Suyash Durendra Pawaskar

Department:

EFFECT OF BORON IN CAST IRON

by

SUYASH SURENDRA PAWASKAR

A THESIS

Presented to the Graduate Faculty of the

MISSOURI UNIVERSITY OF SCIENCE AND TECHNOLOGY

In Partial Fulfillment of the Requirements for the Degree

MASTER OF SCIENCE

in

METALLURGICAL ENGINEERING

2022

Approved by:

Dr. Laura Bartlett, Advisor
Dr. Simon Lekakh
Dr. Ronald O'Malley

PUBLICATION THESIS OPTION

This thesis consists of the following three articles, prepared for conference proceedings in the style used by the Missouri University of Science and Technology:

Paper I, found on pages 14-42 , has been published in 125th American Foundry Society Transactions: Proceedings of the 125th Metalcasting Congress, April 12-22 (2021).

Paper II, found on pages 43-67, has been published in 126th American Foundry Society Transactions: Proceedings of the 126th Metalcasting Congress, April 23-26 (2022).

Paper III, found on pages 68-86, is intended for submission to the International Journal of Metalcasting.

ABSTRACT

Boron, mostly considered a residual element, has started to cause issues in the cast iron foundries by causing a decrease in the strength of pearlitic gray and ductile iron castings. Because of the increase in the use of boron-added steel scrap from automotive steel and a lack of agreement on the critical levels of boron in cast iron, foundries are facing difficulties in controlling the microstructure of gray iron castings when boron is present. The current investigation was designed to analyze the effects of boron in cast irons and predict a mechanism to understand its effects with a vision of finding ways to mitigate and/or control the amount and effect of boron in cast iron. Initially, an experimental study was performed to understand the effect of boron in gray cast iron at four different levels of boron and two carbon equivalents. The study showed that boron acts as a strong carbide stabilizer and ferrite promoting element. The effect of boron on mechanical properties however was seen to vary with carbon equivalent. The experiment was then modified to understand the mutual effect of boron with nitrogen, titanium, and tin to search for a way to mitigate the boron effects. It was observed that nitrogen can help mitigate the effect of boron in gray iron whereas, titanium addition can enhance it. A parallel study to understand the effect of boron in ductile iron was also performed. Boron in ductile iron degrades the graphite sphericity making it into compacted graphite, which led to a deterioration in mechanical properties and significant carbide precipitation, even in casting section sizes as thick as 30mm. The results from the studies indicate that the effect of boron on spherical graphite in ductile iron can be much more severe than in gray iron.

ACKNOWLEDGMENTS

First and foremost, I would like to thank my parents, Mr. Surendra Pawaskar and Mrs. Snehanka Pawaskar for all their love, support, and sacrifices without which I would not have been able to come this far in my life. I would like to extend my deepest gratitude to my advisor and mentor, Dr. Laura Bartlett, for believing in me and providing me with an opportunity to work under her guidance. Apart from being an advisor, she was also a source of immense knowledge and motivation. I cannot thank her enough for all the time and patience she showed during my journey as a graduate student both in and out of the Foundry. I would like to acknowledge the support provided by Dr. Simon Lekakh, who taught me everything I know about cast iron and also helped me become a better researcher and presenter. I am grateful to Dr. Ronald O'Malley, Dr. Mario Buchely, and Dr. Clarissa Wisner who helped me tackle and overcome the obstacles I faced during my research. I would also like to recognize the efforts taken by Mr. Brian Bullock, Mr. Nathan Inskip, Mrs. Teneke Hill, Mrs. Denise Eddings, and Emily Bullock who made sure that all the experimental support was well organized. I would like to express my appreciation to my fellow graduate and undergraduate students for their support during the experiments. I would like to especially thank Michael Piston, Damilola Balogun, Devaprasad Neelkandan, Michael Caubre, and Ryan Van Dyke. I would like to thank my roommates, friends, and family without whom I would not have been able to stand here. Last but not the least, I want to convey my sincere gratitude to my fiancée Tanvi Chalke for being a constant source of emotional and moral support.

TABLE OF CONTENTS

SECTION

LIST OF ILLUSTRATIONS

SECTION Page

PAPER III

LIST OF TABLES

PAPER I

PAPER II

PAPER III

NOMENCLATURE

Symbol	Description
CE	Carbon Equivalent
SCFH	Standard Cubic Feer per Hour
T_L	Liquidus temperature
T_{EMin}	Eutectic minimum temperature (Eutectic undercooling)
T_{EMax}	Eutectic Maximum temperature
V_{Trans}	Velocity of transformation (heat liberation during the eutectoid reaction)
BHN	Brinell Hardness Number
T_{Trans}	Temperature corresponding to highest value of V_{Trans}
γ	Austenite
δ	Ferrite
Fe_2B	Iron boride
T_{Sol}	Solidus temperature
A_3	Eutectoid transformation temperature (Austenite to Ferrite transformation)
C_{Gr}	Graphite
T_{EuLow}	Eutectoid undercooling
ΔR	Eutectoid recalescence
GF1	Graphite Factor 1
GF2	Graphite Factor 2
GF3	Graphite Factor 3

1. INTRODUCTION

1.1. INTRODUCTION TO CAST IRON

Cast iron is an alloy of iron, carbon, and silicon in which carbon is present in excess of that which can be retained in solid solution in austenite at the eutectic temperature. The use of cast irons dates back to 600BC in China, but with the advent of Industrial Revolution and invention of cupola in 17th century, cast irons rapidly outpaced cast steel as an engineering material[1]. Steels contain 2% or less carbon whereas, cast irons contain up to 4% C. All percentages in the following text are expressed as weight percent unless otherwise noted. Given the solubility of C in austenite to be approximately 2%, the excess C then precipitates as graphite with proper inoculation. As a result, cast irons are multiphase alloys that contain more than one constituent in their microstructure.

To understand the solidification in cast irons, it is important to understand the stable iron-graphite and metastable iron-iron carbide phase diagrams (Figure 1.1)[2]. Considering a pure Fe-C binary system, the stable eutectic reaction occurs at 6°C higher than the metastable eutectic reaction. This means, if the iron cools slowly enough, the stable graphite will nucleate with no metastable iron carbide nucleation. However, during cooling, with undercooling as low as 6°C, the metastable reaction will occur and the carbon rich phase will be iron carbide i.e., cementite. Thus, for graphite to nucleate, it becomes necessary to help the system attain equilibrium structure and at industrial cooling rates for feasible productions. The two ways to do this include the use of silicon which changes the binary Fe-C system to a ternary Fe-C-Si system with a wider eutectic freezing range and use of inoculants to aid nucleation of graphite.

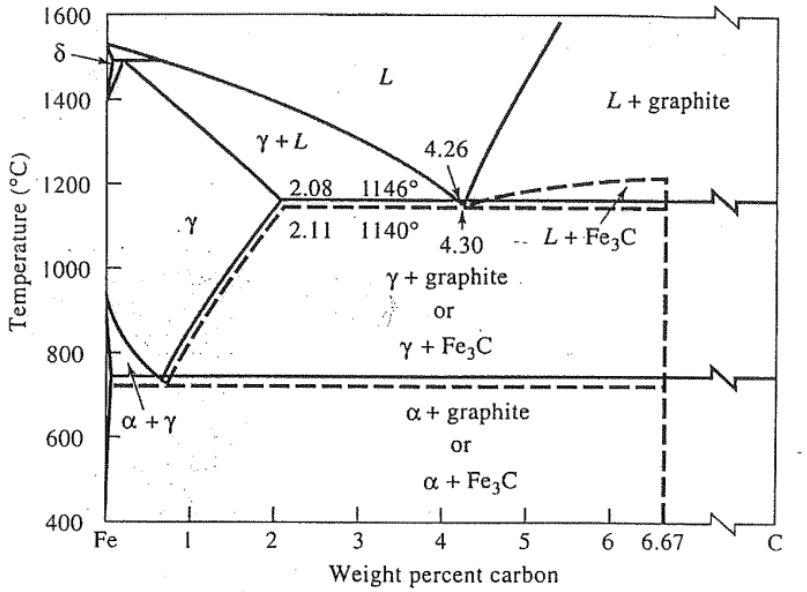

Figure 1.1. Superimposed phase diagrams of the stable Iron-Graphite (solid line) and metastable Iron-Iron carbide (dashed line) phase diagrams[2].

Therefore, graphitic cast irons contain an appreciable amount of silicon, typically 1.0 to 4.0%[1]. The addition of Si in cast iron is pivotal, as it creates a wide eutectic freezing range between the stable graphite eutectic and the metastable carbide eutectic, by decreasing the formation temperature of cementite as shown in Figure 1.2[3]. This increased range decreases the required undercooling for graphite nucleation. Ferrosilicon inoculants with small amounts of reactive elements such as Al, Sr, and Ca help to create complex oxides, silicates and sulfides which serve as a heterogenous nucleus for nucleation of graphite. Si addition also changes the amount of C in the eutectic which causes the eutectic point to shift left. To compensate for this effect, the concept of Carbon Equivalent is used.

Carbon Equivalent in cast irons is expressed in its simplest form as:

$$CE = C\ wt.\% + \frac{Si\ wt.\%}{3} \qquad \ldots(1)$$

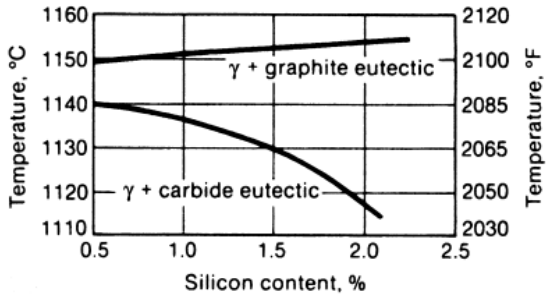

Figure 1.2. Effect of Si on increasing the temperature difference between the stable and metastable eutectic reaction at 4.3 wt.% C[3].

Compared to steels, cast irons have lower melting temperatures, higher fluidity, and are less reactive with mold materials. The high carbon content results in lower density and improved castability, and silicon provides strength in the microstructure. However, the cast iron alloys are not as easily forged, mechanically worked, or as weldable as steel. Depending on the precipitated graphite shape, either as a flake or spheroidal or an intermediate shape, the specific type of cast iron can be defined. The types of cast iron are given below.

1.1.1. Gray Cast Iron. Also known as flake graphite iron, it contains a flake-like structure of graphite, as shown in Figure 1.3. This flake graphite provides gray iron with excellent thermal conductivity and vibration dampening qualities[4]. In return, these flakes however make the iron brittle. Hence most of the gray iron applications deal with stresses induced in compression and as a foundation platform for heavy machinery with high amounts of vibrations.

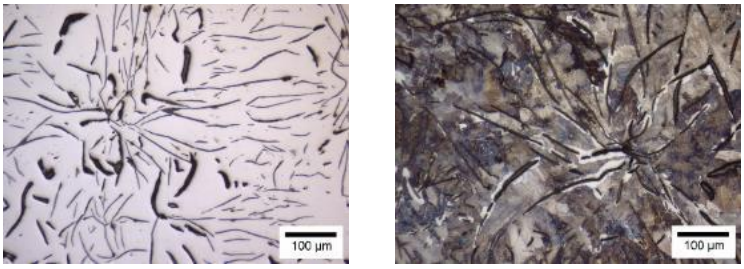

(a) (b)

Figure 1.3. Microstructure representation of gray cast iron casting. (a) Unetched microstructures with graphite in shape of long pointed flakes (black), and (b) Etched microstructure with ferrite (white), lamellar pearlite (dark), and graphite flakes (black).

1.1.2. Ductile Iron. Also known as nodular or spheroidal graphite iron, it contains added Magnesium (0.03%-0.05%) or Cerium[5] to encourage growth of spherical shaped graphite, as shown in Figure 1.4. This spherical graphite provides greater stiffness, strength, ductility, and shock resistance than the flake-shaped gray iron. Different grades of ductile iron can be produced by controlling the matrix structure around the graphite by alloying or heat treatment. Heat treated ductile iron can attain steel-like properties and is called Austempered ductile iron (ADI).

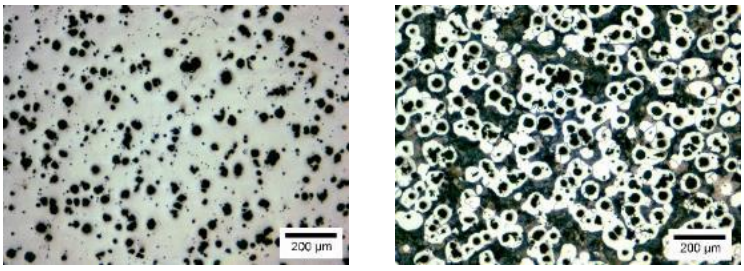

(a) (b)

Figure 1.4. Microstructure representation of ductile iron casting. (a) Unetched microstructures with spherical graphite (black), and (b) Etched microstructure showing a typical bull's eye pattern with spherical graphite (black) surrounded by ferrite (white), and lamellar pearlite (dark).

1.1.3. Compacted Graphite Iron. This type of cast iron was developed to combine the properties of gray and ductile iron for applications which simultaneously deal with thermal and mechanical loads like engine blocks[6]. It also contains Mg, but less than 0.03%. Consequently, an intermediate microstructure between the flake graphite of gray iron and spherical graphite of ductile iron, as shown in Figure 1.5. It has good castability of gray iron but has higher strength and ductility than the latter.

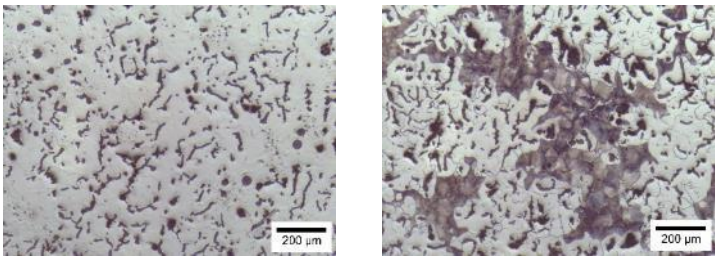

(a) (b)

Figure 1.5. Microstructure representation of compacted graphite iron casting. (a) Unetched microstructures with a mix of spherical and vermicular graphite, and (b) Etched microstructure graphite (black) surrounded by ferrite (white), and lamellar pearlite (dark).

1.1.4. White Iron. This type of iron contains excess amounts of iron carbide (Fe_3C) also known as cementite. It is hard and brittle but has high wear resistance. Cementite precipitation in grey or ductile iron is unintentional and a result of insufficient inoculation, thin section sizes, and/or high cooling rates. Despite of this, white iron castings find a lot of applications where high wear and abrasion resistance is required, like ball mills, crushers, and grinders[7]. White iron is intentionally alloyed with carbide stabilizers like Cr, B and Mo[1]. Since the C is present as carbides and not as graphite, its density is higher**.** Representative images for white iron are shown in Figure 1.6

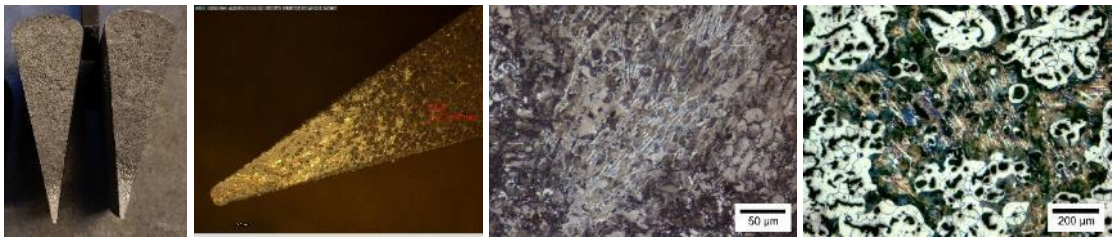

(a) (b) (c) (d)

Figure 1.6. Microstructure representation of white iron. (a) Tips of the chill wedges forming white iron, and (b) Magnified image of the chill wedge tip, (c) White iron formed in a grey iron casting, and (d) White iron formed in a ductile iron casting.

1.1.5. Malleable Iron. Malleable iron is the type of iron obtained when white iron is subjected to solid-state transformations during heat treatments[8]. At the heat treatment temperatures (approximately 900°C), the carbides dissociate into austenite and irregularly shaped graphite called temper carbon as shown in Figure 1.7[1]. Depending on the cooling rates, a wide range of properties can be achieved as ferritic, pearlitic, or martensitic malleable iron.

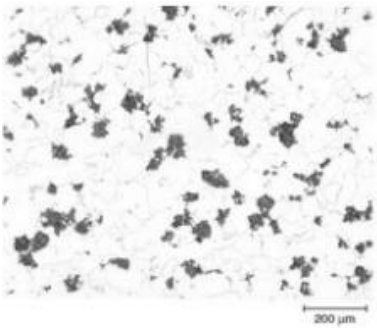

Figure 1.7. Microstructure representation of a ferritic malleable iron casting with irregularly shaped graphite called temper carbon (black) [1].

1.2. PROJECT PURPOSE AND OVERVIEW

In cast iron, Boron is considered a residual element. Foundries using steel scraps for their production are facing issues with a rise in B content in their iron due to the increasing use of B-added steel in the automotive industries. Foundries started facing issues of reduction in mechanical properties of the casting with an increase in B content. A term called 'soft' pearlitic casting was coined by the foundries due to this unprecedented decrease in the mechanical properties of the castings. B was suggested to counteract the effect of perlite stabilizing elements like Mn, and Cu, which are responsible for the mechanical properties of the casting[1]. This has become a major concern for the foundries as they are left to cope with B contamination issues accompanied by a reduction in the quality of castings.

The sources of B in cast iron are traced back to the use of B-added steel scraps as a raw material. The sudden rise in the use of B-added steels, infamously termed as 'poor man's Interstitial Free steels' in the automotive industries in 2007[9] ensued a rise in B-added steel scraps. Along with steel scraps, B can enter the iron chemistry through the refractory linings used in the furnaces or ladle linings used to pour the iron. The use of enameled scraps like cooker handles, and saucepans can also serve as a source of B in cast iron if not monitored closely [10]. Although scrap quality control can be done to avoid some sources of B, the refractory source of B has not been dealt with yet.

As B is considered a trace element, the safe limit of B has been debatable. This is also supplemented by the fact that literature dealing with the effects of B is inconsistent and varied. Not only the individual effect but the synergistic effect of B with pearlite stabilizing elements like Mn, Cu, and Sn and minor elements like N, Ti, and Al is not

studied enough to create a solution for mitigating the detrimental effects of B on microstructure and mechanical properties. This creates a necessity to understand and precisely quantify the effects of B and eventually figure out a safe level of B in cast iron in general. The purpose of this study will be to quantify the effects of B in cast iron starting with gray iron to answer the questions raised above. The study will also attempt to answer a safe limit of B in cast iron along with a mitigation strategy of this effect to deal with the unintentional entry of B in the iron. The outcome of this project is intended to reveal the effects and determine the mechanism of B on microstructure, and mechanical properties of gray cast iron and eventually suggest a way to mitigate these effects.

2. LITERATURE REVIEW

As previously mentioned, the effect of B in cast iron is not completely understood. The studies conducted had varied ranges of B and hence a clear trend of the B effect could not be stated. Boron in steel is added purposefully as it can help enhance the hardenability of steel. The use of B-added steels in various automotive applications, gas, and oil pipelines has increased because B-added steels can replace the expensive high-carbon low alloy steel sheets with a cheaper alternative [11]. These B-added steels become a source of B in cast iron when used as scrap for melting. In cast irons, B is not added intentionally, rather it is considered a trace element.

The effect of B on cast iron properties started to be reported in the 1940s. Schwartz [12], showed an improved annealing behavior of malleable irons with a B content up to 0.003% by stabilizing carbides. Bastien and Guillet [13] studied the effect of B in cast iron by varying B content from 0.046% to 0.385%. The chemical composition of cast iron studied was 3.09 to 3.65% C, 1.45% Si, 0.45% Mn, 0.06% P, and 0.01% S. Their study showed that the graphite particles decreased with increasing B with the most noticeable effect seen at 0.18% B. Along with the reduction in particle count, the shape of the graphite showed variations as well. The graphite flakes for the B-added cast irons became shorter, thinner, and concentrated in colonies. The flake edges became rounded as compared to the usually pointed edges. According to the current graphite flake shape characterization, the flakes could well be classified as type D graphite flakes[14]. These D-types flakes would then result in reduced mechanical properties.

Studies conducted by Alexander [15] on cast irons showed a proportional increase in carbides with B levels. The cooling curve analysis in this study indicated a progressive increase in undercooling effects with increasing B. It also stated that the difference between the apparent liquidus and solidus reduced thus indicating an approach towards the eutectic composition. Brinell hardness increased with increasing B. Vickers hardness tests on the chill plates also showed an increase in hardness with increasing B. An increase in B also showed a negative effect on the graphite flake amount and size. With 0.29% B additions, the matrix was carbidic having islands of fine pearlite. This paper also hypothesized those carbides formed due to B addition might have a Fe(C, B) complex rather than the usual Fe_3C. Another important finding from this paper was that B cannot be taken out from the metal by remelting. Thus, the only conceivable way to reduce B in cast irons is by dilution.

According to the US patent 2,579,452 [16], in a study of preparing malleable iron with Bi and B additions, the addition of B as a carbide stabilizer improves the properties of the prepared malleable iron. Also, B acts as a graphitization promoter decreasing the time required for annealing. Graphitization is the process of forming graphite nodules called tempered carbon in malleable iron during the annealing of white iron. However, large B additions particularly, in high-C irons can lead to precipitation of dendritic temper carbon which is detrimental to the properties of malleable iron.

The carbide stabilizing effect of B can be of use in white iron castings. Studies conducted by Bedolla-Jacuinde [17] suggest that increase in B content can considerably increase the wear resistance in 17Cr-3C-1Ni-1Mo white iron. B helps in promoting Cr-rich M_7C_3 eutectic carbides instead of the low C and Cr containing $M_{23}(C, B)_6$ carbides and also increased the carbide volume fraction from 27.1% to 53.8%. However, with the

application of heat treatment, the higher B content iron showed a decrease in wear resistance when compared with irons with a lower B content.

According to the Sorel metal handbook for ductile irons [18], B is a strong carbide stabilizer. As little as 0.002% B can result in the formation of intercellular carbides which can adversely affect the mechanical properties of cast iron. B in levels of 0.01% can reduce the ductility from 14% to as low as 1%, which can be attributed to the formation of carbides. The carbides formed due to B are extremely stable and can resist annealing. B can also reduce the effects of pearlite promoting elements like Cu and reduce the hardness of the casting. Hence the limit of B in pearlitic iron is as low as 0.0006%. Another study conducted by Mitra [19] on ductile iron pipes suggests that B up to 200ppm does not have any perceptible deleterious effects on the performance of DI pipes. It also suggests that B-added DI (up to 200ppm) pipes show better machinability and a favorable combination of strength, ductility, and hardness when compared to non-B-containing pipes.

A study conducted on gray cast iron by Knud [20], shed some light on the combined effect of B and N. The study predicted and proved that hexagonal BN has a crystal structure similar to the graphite and in theory would help in the nucleation of graphite. The study also stated that the age-hardening effect of N in cast iron due to the formation of a stable supersaturated Ferrite Fe_4N can be reduced with B additions to form BN.

The graphite nucleation theory by Knud is supported by a study performed in a US patent in 2006 [21] on ductile iron doped with B, which stated that the BN formed can serve as a nucleus for graphite precipitation. The addition of up to 80ppm B increased graphite nodule count. This increase in nodule-count also proved to improve the annealing capabilities of the ductile iron. This study also commented on the carbide forming

properties of B. Comparing >150ppm B-added and non-B-added chemistries tailored to promote carbides, the B-added chemistries showed a higher amount of inter-cellular carbides than non-B-added ones. These boron-containing carbides are very stable and difficult to remove using normal heat treatments. However, in the same paper, the annealibility of carbides and pearlite increased in the B-added samples which is a result of increased nodule count in the B-added samples.

In the literature survey conducted by Naro and Wallace [22], B is described as a very strong carbide stabilizer in ductile iron. The effect of B on microstructure and consequently on mechanical properties is however conflicting. 20ppm B addition in a pearlitic ductile iron showed varying effects on pearlite content and mechanical properties. While in one casting the amount of pearlite reduced from 90% to 40% by volume accompanying an increase in ferrite, the other casting seems to show no effect on pearlite volume fraction and instead increased the Brinell hardness values by 10%. Although both the casting chemistries were identical, the exact nature of the B mechanism could not be understood then. In a technical bulletin published by the Ductile Iron Society [23], the ferritic ductile iron castings were unaffected by the addition of B whereas the pearlitic castings showed a decrease in mechanical properties and hardness with a B addition as low as 5 to 20ppm. The quantity of pearlite stabilizers like Cu and Sn was doubled to successfully control the effect of B in these pearlitic castings. In another study conducted by a foundry, the hardness of the pearlitic castings returned to the normal (200-210 BHN) when the B dropped to 17ppm and increased up to 230 BHN when B dropped below 6ppm.

Overall, most of the literature cited here suggested B as a strong carbide forming agent. B also affects the graphite nucleation and size negatively in both gray and ductile

iron. However, the effect on other phases like pearlite and ferrite is confusing. Another point to be noted from all these studies is that the amount of B studied is inconsistent, and thus the question of what would be the limit of B in the iron is raised. Along with this, the effect of B is different even with identical iron chemistry. This suggests that the effect of B might just not be individual but rather a combined effect with other alloying elements which has not been studied as of yet. Also, because there was no significant B loss during remelting of B-added cast irons, it becomes vital to search for a way to mitigate the B effect since the only countermeasure left to deal with the B contaminations is charge dilution.

PAPER

I. EFFECTS OF BORON IN CLASS-30 GRAY IRON

S. Pawaskar, L.N. Bartlett, S. Lekakh

Department of Material Science and Engineering, Missouri University of Science and Technology, Rolla, MO 65409

Keywords: cast iron, boron, thermal analysis, structure, mechanical properties

ABSTRACT

Increasing usage of boron in automotive steels progressively contaminates cast iron charge mixtures. There are many controversial opinions about the boron effect on the structure and properties of cast iron and no agreement about acceptable critical concentrations of this element in cast iron. Therefore, an experimental study was performed to uncover the effects of boron in Class-30 gray iron. Ferro-boron additions were used to increase boron up to 130 ppm in several laboratory heats. Thermal analysis was utilized to determine the effect of boron on phase transformations during solidification and eutectoid transformation. Mechanical property tests and microstructural analysis were conducted to determine the effect of boron at different carbon equivalents. The results showed that the effect of boron in cast iron was significantly affected by carbon equivalent. A preliminary discussion about the mechanisms of boron effects on phase transformations and properties of gray cast iron is presented.

1. INTRODUCTION

Good casting capabilities, sound mechanical and physical properties, simplicity in production, and the lost cost makes cast iron very versatile in industrial applications. Although most of these properties are affected by the chemical content of elements like C, Si, Mn, and Cr the trace elements in cast iron also have their fair share of contributions towards enhancing or deteriorating the properties of the casting. One of these trace elements which has been causing some problems for the Iron foundries is boron (B).

During the last decade, the addition of B to automotive-grade steel has increased. The hardenability provided by B has found many applications in the automotive panel class steels. This B-added steel then finds its way through scraps into the cast iron charges. Complaints have been received from the gray iron foundries about intended quality control issues with such B-added material. Another source of B in gray iron can be the fresh furnace linings.

The effect of B in gray iron is not very precisely studied. B is known as a strong carbide stabilizer. According to Ankamma et.al [1], the presence of B above 550ppm can be disastrous to the iron in terms of chill and cracking problems in thin section castings. It can also cause the formation of undesired graphite flake structures like type D and reduce the strength of the material. Smaller graphite structures like type D can create small carbon diffusion distances from the matrix to the graphite flakes ultimately creating regions of ferrite which can adversely affect the mechanical properties of gray iron. To avoid chill, B is recommended to be maintained under 50ppm.

Another effect of B is that it is a ferrite stabilizer [2]. Its presence can cause severe effects on pearlitic grades of gray iron. B may counteract with pearlite stabilizing elements like Cu and Mn resulting in 'soft' pearlitic castings. Cu alloying tends to segregate to the austenite-graphite interfaces and prevents the diffusion of carbon, resulting in the transformation of austenite into pearlite. However, B might accumulate around graphite and disrupt the effect of Cu. This segregation of B was confirmed by other authors using secondary ion mass spectroscopy [3]. Boron was detected surrounding graphite nodules in ductile iron. The B content used in that study was 50 to 70ppm. The ferrite stabilizing effect of B was also shown in ductile iron [4] where specimens higher in boron were found to have an increased amount of free ferrite and consequently a reduction in pearlite.

The effect of B on austenite is said to be similar to that of Ti, and B additions can stabilize nitrides that serve as substrates for the nucleation of austenite [5]. Another effect can be an increase in the undercooling and the reduction of graphite nucleation potential. The effect of B on graphite flake size was studied by Alexander et.al [6]. The study concluded that the graphite flake size reduces for higher additions of B. However, it should also be noted that this study dealt with B levels of 0.003wt.% to as high as 0.33wt.%. In the same study, increasing B content was seen to reduce the temperature gap between liquidus and solidus temperatures and increase the undercooling effects.

The purpose of this investigation, funded by the American Foundry Society, is to provide experimental information on the effects of B in gray iron of different classes. This article reports Phase-I results dedicated to Class-30 cast iron. The properties under investigation were thermal analysis parameters, microstructure, chilling tendency, strength, and hardness.

2. METHODOLOGY

Two types of Class 30 GI heats were cast in the laboratory. Heats were performed in a 200lbs induction furnace. The first heat was planned to be a high carbon equivalent (CE) heat with a CE target of 4.3-4.4 (high-CE) and the second with a CE target of 4.0-4.1 (medium-CE). Future studies will be performed with low CE also (3.8-3.9) The effect of B was studied across four different levels of B addition for the same chemistry. The initial chemistry had no B addition. Then the B was intentionally added in levels of 20ppm, 40ppm, and 100ppm. The B addition was done in the induction furnace itself to enhance the B recovery [6].

The charge for both the heats consisted of high purity induction iron ingots, ferrosilicon, ferromanganese, metallic chromium, high purity graphite, and foundry returns from our foundry sponsor (Table 1). An argon cover at a flow rate of 25 SCFH was used to increase recovery rates. The target chemistries for high-CE and medium-CE heats are given in the Table. 2.

Table 1. Chemical composition (wt.%) of the charge materials used for the heats.

Charge Source	C	Si	B	Cr	Mn	Cu	P	S
Waupaca foundry returns	3.47	2.13	0.0004	0.21	0.57	0.21	0.028	0.086
Induction iron	0.0017	0.002	0.0001	0.01	0.01	0.002	0.005	0.0025
Ferro-Silicon (Fe75Si)	--	75	--	--	--	--	--	--
Ferro-B (Fe18B)	0.26	0.58	18.52	--	--	--	0.028	0.003
Desulco graphite	99.99	--	--	--	--	--	--	--
Inoculant*	--	70	--	--	--	--	--	--
Metallic chrome	-	-	--	98	--	--	--	--
Ferro-Manganese	1.00	1.00	--	--	76	--	--	--

* Inoculant composition: Si: 70wt.%; Al: 0.17wt.%; Sr: 0.76wt.%; Co: 0.039wt.%

Table 2. Target chemistries (wt.%) for the heats.

Heat	C	Si	CE	B (ppm)	Cr	Mn
High-CE heat	3.40	2.5 - 2.6	4.3	2/20/40/100	0.10 - 0.15	0.20 – 0.30
Medium-CE heat	3.35	1.8 - 1.9[#]	4.0	2/20/40/100	0.15 - 0.20	0.45 – 0.55

[#] Si target before inoculation

To check the CE in the melt, thermal analysis with tellurium (Te) added cups were used. The tapping temperature for the heat was maintained between 1360-1380°C. The metal was tapped into 22lbs hand ladles. A total of four chemistries were planned for the heats with varying B additions. The 1st chemistry was no B-added, 2nd 20ppm. 3rd 40ppm and the 4th 100ppm B additions. Each chemistry required two hand ladles. The inoculation was done for each hand ladle during tapping. The inoculant used for the heats was Superseed (Si 70%) and was taken as 0.2% weight of each hand ladle capacity.

In order to check the chemical composition of each chemistry, two types of samples were taken: an immersion sample and a sample poured into a Cu chill mold. To understand the B effect on mechanical properties of gray iron, multiple molds were poured for each chemistry, including a step block, ASTM A48 B-bar molds, and a chill wedge. The step block (Figure 1) had four steps 5, 10, 20, and 30mm. A total of 6 B-bar samples were obtained from each chemistry.

Thermal analysis was performed by obtaining the cooling curves from ATAS software using non-Te coated cups. The obtained cooling curves were used to analyze the effects of B on eutectic and eutectoid reactions. The variation in critical parameters of the cooling curves was studied as suggested in the work of J. Sertucha et.al [7] and Stefanescu et.al [8] to understand the effect of B on solidification and solid-state transformations of gray iron. The nomenclature of the used parameters is shown in Figure 2[8].

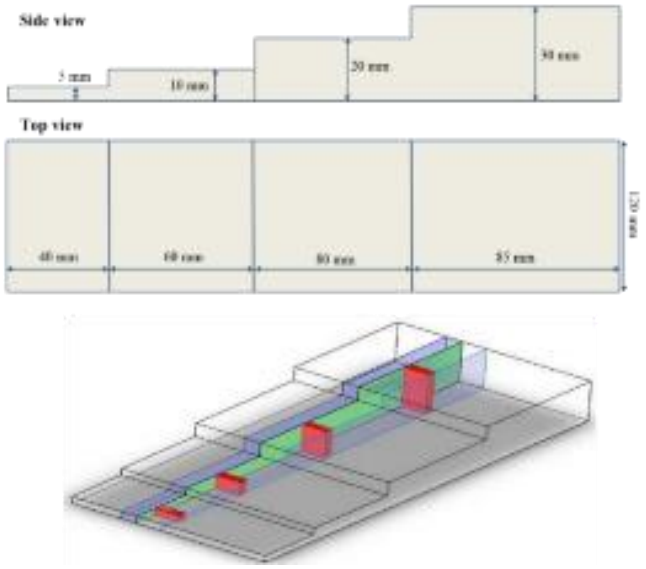

Figure 1. Side, top, and isometric view of step block. The red area was used for metallographic analysis and hardness was measured in the green section.

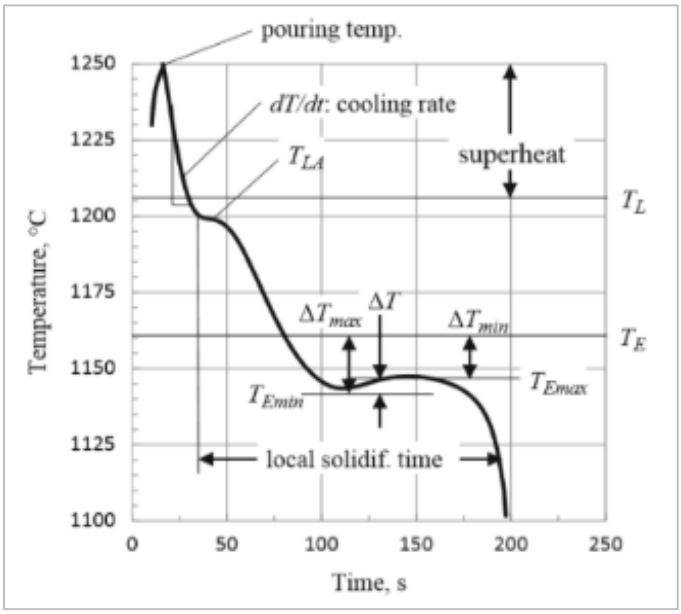

Figure 2. Nomenclature of the used parameters of thermal analysis (from the ATAS software) [8].

Specimens for optical metallography were taken from the step blocks. The specimens were sectioned from the center of the step block and the center of each step as shown in (Figure1). Polishing for the optical metallography was performed by standard metallographic techniques. Unetched and etched images were taken from each specimen. 3% Nital was used as the etchant. For quantifying the matrix and graphite flake structure, images were analyzed using ImageJ software.

The chemical composition analysis was done using optical emission arc spectroscopy (OES) and combustion analysis using a commercial C/S and O/N analyzer. The B content of the standards used is given in Table. 3. Tensile tests were performed on a 250kN servo-hydraulic load frame in accordance with the ASTM A-48[9]. Test bar specifications used for the tensile test were according to the B type test bar. The tensile test was performed at a strain rate of 0.02mm/s. Hardness tests were performed on a Brinell hardness tester, and the tests were performed following the ASTM E10-18[10]. Standard hardness blocks were tested before and after the test of actual specimens. Hardness tests were repeated four times per sample and only for the 20mm and 30mm steps of the step blocks.

Table 3. OES calibration for B (ppm). OES values are the average of six measurements.

Standard Name	Certified B (ppm)	OES B (ppm)
BS 4C	2	1
34A	76	72
RN 14/39	30	38
RG 14/161	400	400

3. RESULTS

The chemical compositions of the heats obtained from the OES are given in Table. 3. To check the B content as low as possible, a 2ppm B standard was used. All the standards were tested before testing the actual specimens. The actual chemistries of the heats were close to the target chemistry. It should be noted that Cr and Mn content ranged from 0.12wt.% to 0.20wt.% and 0.30 wt.% to 0.50wt.%, respectively. Si was reduced from 2.7 wt.% to 2.0 wt.% from the high-CE heat to medium-CE heat. The target carbon content was higher for both the heats by 0.1wt.%. In this article, B additions were used for data analysis. Future comparisons will be performed for heats with different CE using actual B concentrations.

Table 4. Chemical compositions for the two heats (wt.%).

Heat	Ladle	B-added	C*	Si	CE	B (ppm)	Cr	Mn	Cu	P	S*	Sn
High-CE Heat	1A	No B-added	3.56	2.70	4.46	22	0.12	0.29	0.14	0.028	0.064	0.013
	1B	20	3.52	2.77	4.44	38	0.12	0.29	0.13	0.028	0.071	0.013
	1C	40	3.47	2.69	4.37	56	0.12	0.29	0.13	0.028	0.071	0.014
	1D	100	3.53	2.67	4.42	113	0.12	0.29	0.14	0.030	0.074	0.014
Medium-CE Heat	2A	No B-added	3.45	2.05	4.13	5	0.21	0.58	0.034	0.025	0.020	0.009
	2B	20	3.44	2.07	4.13	25	0.21	0.58	0.036	0.023	0.019	0.008
	2C	40	3.41	2.03	4.09	46	0.21	0.58	0.034	0.024	0.017	0.008
	2D	100	3.39	2.07	4.08	98	0.21	0.59	0.035	0.024	0.018	0.008

* C, and S readings taken from commercial C, S, N, O analyzer

The thermal analysis parameters obtained from ATAS software using the non-Te cup are shown in Table. 5. It can be clearly seen from the data that the liquidus temperature

(T_L) rises as B content increases. This is true for both the heats irrespective of the CE. Another effect that can be noted is that the eutectic minimum temperature (T_{Emin}) dropped as the B content increased. The eutectic cooling curves for high-CE heat are shown in Figure 3 and the cooling curve for the medium-CE heat is shown in Figure 4. The observations from Table. 5 are clearly visible in these graphs.

Table 5. Thermal analysis data obtained from ATAS software for both the heats.

Heat	High-CE Heat				Medium-CE Heat			
Chemistry	No B-added	20ppm B-added	40ppm B-added	100ppm B-added	No B-added	20ppm B-added	40ppm B-added	100ppm B-added
Liquidus Temp, T_L (˚C)	1157.3	1157.3	1158.4	1159.3	1193.3	1195.8	1199.3	1202.2
Eutectic Start (˚C)	1154.9	1154.5	1155.5	1155.1	1176.9	1178.6	1180.3	1180.9
Eutectic Minimum, T_{Emin} (˚C)	1151.4	1149.7	1151.4	1150.3	1147.5	1146.3	1146.7	1144.8
Eutectic Maximum, T_{Emax} (˚C)	1154.2	1153.2	1154.8	1153.8	1150.5	1150.1	1149.9	1148.2
Solidus Temp, T_{Sol} (˚C)	1109.4	-	1108	1108.4	1100.8	1108.5	1106	1107
Recalescence, ΔT (˚C)	2.8	3.5	3.4	3.5	3.0	3.8	3.2	3.4
Graphite Factor 1	70	-	69	75	72	75	62	71
Graphite Factor 2	20	-	20	17	24	19	32	35

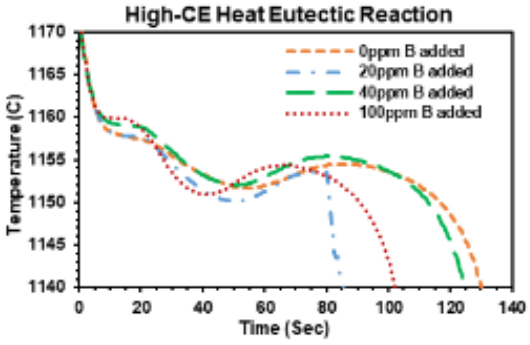

Figure 3. Eutectic cooling curve for high-CE heat.

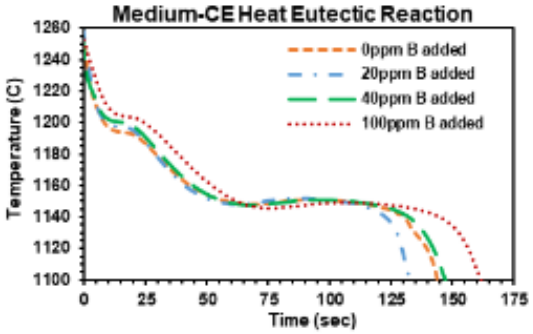

Figure 4. Eutectic cooling curve for medium-CE heat.

The cooling curves shown in Figure 5 and Figure 6 represent the eutectoid reactions for high-CE and medium-CE heats respectively. The red-dotted line represents the V_{Trans} for the eutectoid reactions. Eutectoid parameters like temperatures of eutectoid low and the eutectoid recalescence were analyzed to understand the effect of B in solid-state transformation reactions. In addition, the 1st derivative of the cooling curve was plotted against the temperature for the eutectic and eutectoid reactions to analyze the change in cooling rates related to the latent heat liberation and the eutectoid parameters like V_{Trans}. These graphs are presented in the discussion part of this article.

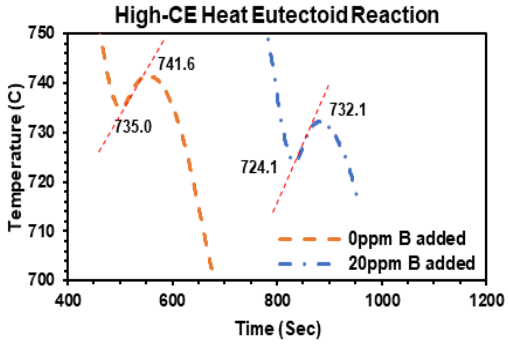

Figure 5. Eutectoid reaction curve for high-CE heat.

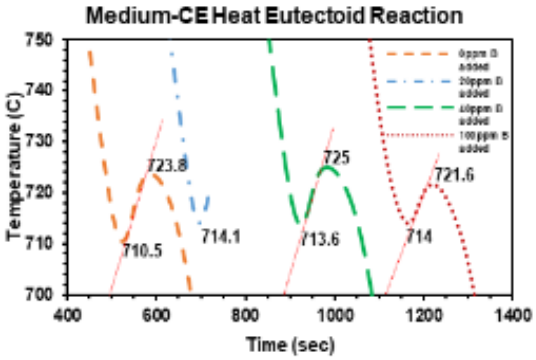

Figure 6. Eutectoid reaction curve for medium-CE heat.

The unetched and etched microstructures obtained from the 30mm step of high-CE heat are shown in Figure 7 and Figure 8. Higher ferrite content is observed in the matrix of higher B specimens. Although image 1A in Figure 7 seems to have a higher ferrite content, it must be noted that the area represented in the metallographic analysis is very limited and thus cannot be accurately considered as a complete representation of the structure. The unetched and etched microstructures from the 30mm step of the medium-CE heat are shown in Figure 9 and Figure 10. No considerable difference between the specimens can be seen. Although it can be noticed that the ferrite content is higher in high-CE heat as compared to medium-CE heat which is understood because of the higher Si content in the former. Analysis of the microstructure images from the smaller steps i.e., 10mm and 20mm of both the heats was also performed. As the cooling rates in the smaller steps are higher, the microstructure was mainly pearlite, and the ferrite content of the microstructure was low as compared to the 30mm step. The etched images from the 20mm step for the high-CE and medium-CE are given in Figure 11 and Figure 12, respectively. Similarly, microstructure images from the 10mm step for the high-CE and medium-CE are shown in Figure 13 and Figure 14, respectively.

The chill wedge images from high-CE and medium-CE heat are shown in Figure 15 and Figure 16, respectively. The microstructure analysis of the chill wedge was done in five areas, the tip and then at 5mm increments up to 20mm from the tip. It is clearly shown that the chill depth increases for higher B content for both the heats. The chill depth increased from 7.28mm to 13.1mm as the B content increased. Carbide structures are visible further away from the tip in higher B content for both of the heats. Carbide structures in high-CE heat are only seen in the microstructural analysis. The carbide can be seen at a distance of 5mm in the higher B sample, whereas the low B samples do not have carbide structures beyond the chill tip portion. This is a clear indicator that B acts as a carbide stabilizer.

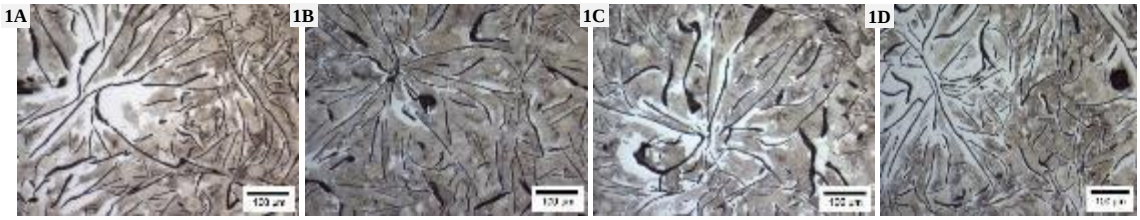

Figure 7. Etched microstructures taken from the 30mm step of the high-CE heat: 1A - no B-added, 1B - 20 ppm, 1C - 40 ppm, and 1D - 100 ppm B-added.

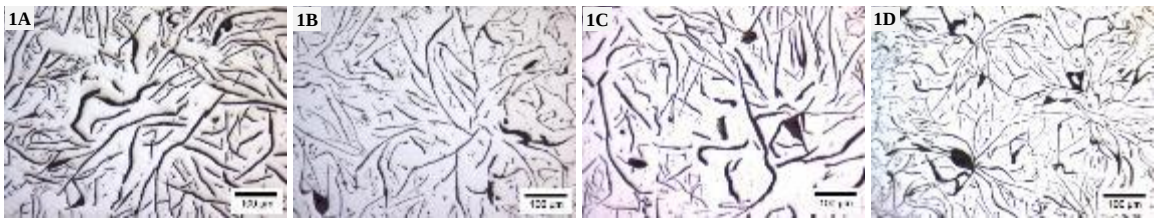

Figure 8. Unetched microstructures taken from the 30mm step of the high-CE heat: 1A - no B-added, 1B - 20 ppm, 1C - 40 ppm, and 1D - 100 ppm B-added.

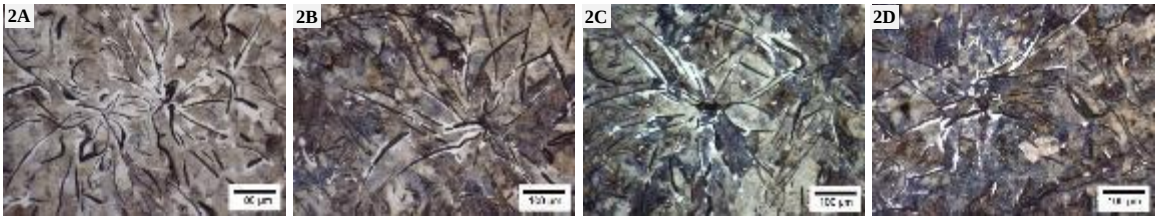

Figure 9. Etched microstructures taken from the 30mm step of the medium-CE heat: 2A - no B-added, 2B - 20 ppm, 2C - 40 ppm, and 2D - 100 ppm B-added.

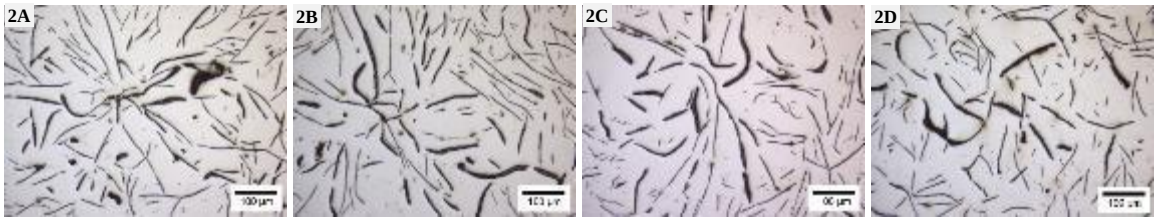

Figure 10. Unetched microstructures taken from the 30mm step of the medium-CE heat: 2A - no B-added, 2B - 20 ppm, 2C - 40 ppm, and 2D - 100 ppm B-added.

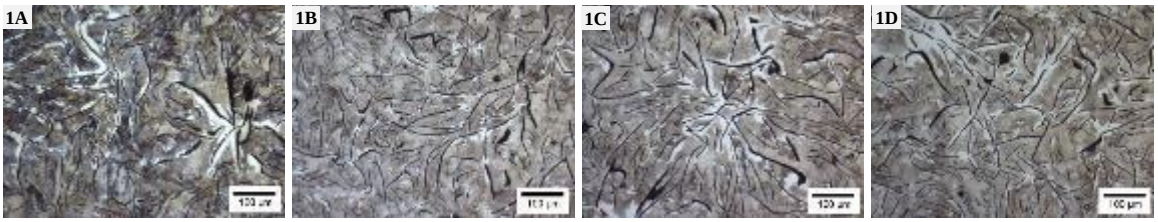

Figure 11. Etched microstructures taken from the 20mm step of the high-CE heat: 1A - no B-added, 1B - 20 ppm, 1C - 40 ppm, and 1D - 100 ppm B-added.

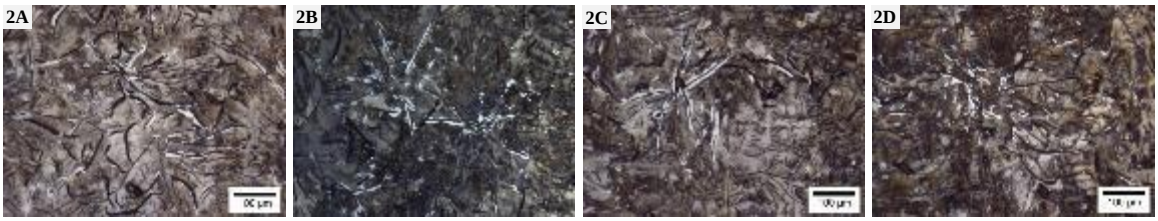

Figure 12. Etched microstructures taken from the 20mm step of the medium-CE heat: 2A - no B-added, 2B - 20 ppm, 2C - 40 ppm, and 2D - 100 ppm B-added.

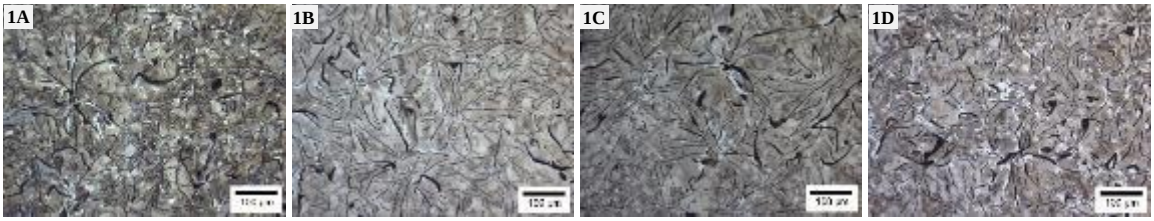

Figure 13. Etched microstructures taken from the 10mm step of the high-CE heat: 1A - no B-added, 1B - 20 ppm, 1C - 40 ppm, and 1D - 100 ppm B-added.

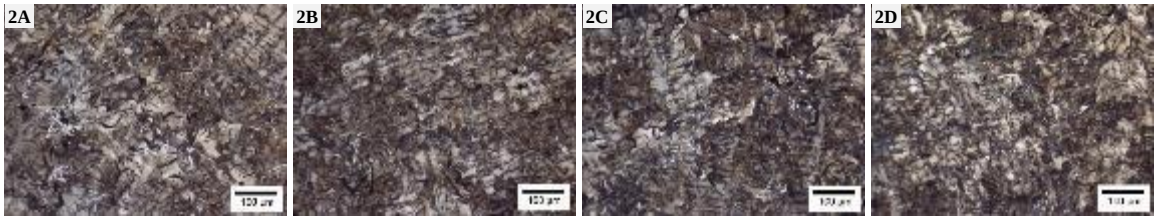

Figure 14. Etched microstructures taken from the 10mm step of the medium-CE heat: 2A - no B-added, 2B - 20 ppm, 2C - 40 ppm, and 2D - 100 ppm B-added.

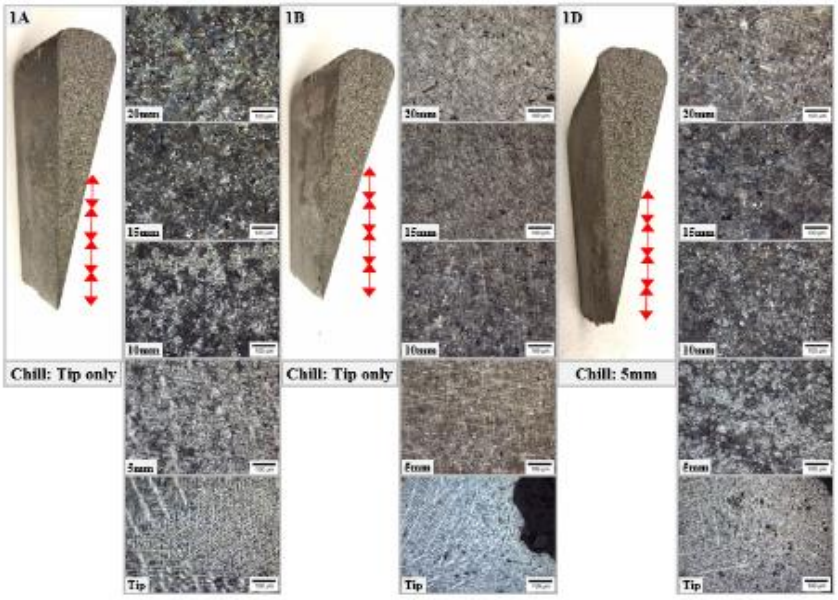

Figure 15. High-CE heat chill wedge fractures and etched microstructures taken at the chill tip and regions at 5mm increments up to 20mm: 1A - no B-added, 1B - 20 ppm, and 1D - 100 ppm B-added. The chill tip is not visible in the images.

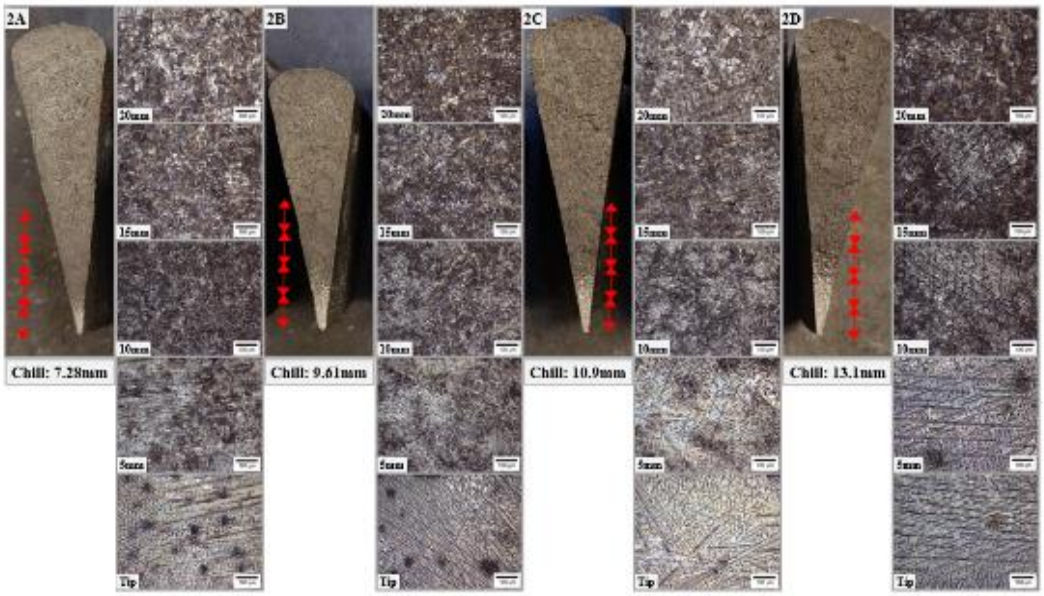

Figure 16. Medium-CE heat chill wedge fractures and etched microstructures taken at the chill tip and regions at 5mm increments up to 20mm: 2A - no B-added, 2B - 20 ppm, 2C - 40 ppm, and 2D - 100 ppm B-added. The chill tip is visible in the images.

The tensile results from the heats are given in Table. 6. The ultimate tensile strength (UTS) of high-CE heat is lower than that of medium-CE heat and this is due to the high levels of Si. A clear trend of increasing tensile strength of the specimens is shown for the medium-CE heat, but this is not the case for high-CE heat. In this heat, the UTS rises for the initial B addition and then decreases when B additions increase. The hardness results are shown in Table. 7 and were in affirmation with the tensile results. The hardness values for the high-CE heat are lower.

Table 6. Ultimate tensile strengths (ksi) as a function of boron for both heats.

Heat	B-added, ppm	Test 1	Test 2	Test 3	Test 4	Test 5	Test 6	Average TS	Std Dev
High-CE heat (CE = 4.43)	No B-added	20.2	21.0	20.7	20.9	20.6	20.3	20.6	0.32
	20	22.9	23.3	22.4	22.9	22.4	22.8	22.8	0.33
	40	22.4	22.8	21.7	21.2	22.0	22.3	22.1	0.58
	100	20.4	21.6	21.4	20.4	21.8	21.1	21.1	0.60
Medium-CE heat (CE = 4.1)	No B-added	30.6	30.6	27.2	28.5	28.5	28.1	28.9	1.4
	20	32.6	33	28.8	30.3	29.2	28.8	30.5	1.9
	40	33.5	32.7	30	29.8	29.3	29.4	30.8	1.8
	100	33.8	34.9	30.6	30.9	31.3	30.9	32.1	1.8

Table 7. Hardness (BHN) results as a function of boron for both the heat.

Heat	Step	No B-added	20ppm B-added	40ppm B-added	100ppm B-added
High-CE heat (CE = 4.43)	Step 4 (30mm)	125± 1	135 ± 5	126 ± 2	125 ± 3
	Step 3 (20mm)	125 ± 5	137 ± 6	128 ± 5	133 ± 2
Medium-CE heat (CE = 4.1)	Step 4 (30mm)	143 ± 2	148 ± 3	153 ± 4	162 ± 3
	Step 3 (20mm)	150 ± 2	153 ± 1	155 ± 5	166 ± 3

4. DISCUSSION

Two cast irons with high and medium levels of CE were produced with different levels of boron. This study intends to evaluate the specific effect of B additions on phase transformations, microstructure, and mechanical properties of gray iron at different CE levels.

4.1. SOLIDIFICATION

Both cast irons were hypoeutectic, and solidification started with primary austenite. The cooling curves from both the heats (Figure 3 and Figure 4) show a clearly indicated trend of increasing liquidus temperature with B additions, which relates to the stimulation of austenite solidification. The effect of B addition on the eutectic transformation depended on CE. It is known that the undercooling of the eutectic reaction is related to the nucleation of graphite and higher B content makes it slightly difficult for graphite nucleation and stabilizes austenite. Plots of the 1st derivative of the cooling curve as a function of temperature in Figure 17 and Figure 18 show that the rightmost peak in the plot marks the austenite liquidus temperature. The loop in the graph is the eutectic recalescence. The leftmost point of the loop is the eutectic low temperature, T_{Emin}, while the rightmost point of the loop is the eutectic high, T_{Emax}. The diameter of the loop will give the eutectic recalescence. It is visible that the temperature difference between the austenite liquidus and the eutectic low rises with B content. This trend is observed in both the heats (Figure 17 and Figure 18). The difference between T_L and T_{Emin} is shown in Table. 8.

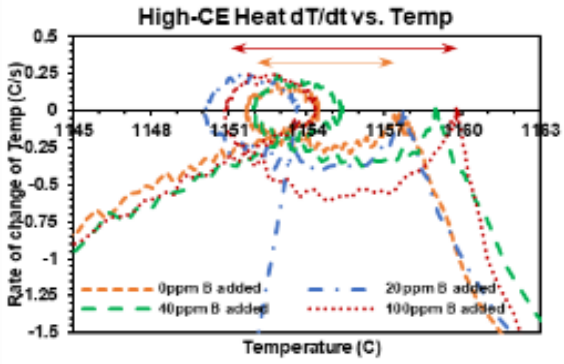

Figure 17. 1st derivative of the cooling curve plotted against temperature for high-CE heat for the solidification. The difference between the T_L and T_{Emin} is highlighted by arrows.

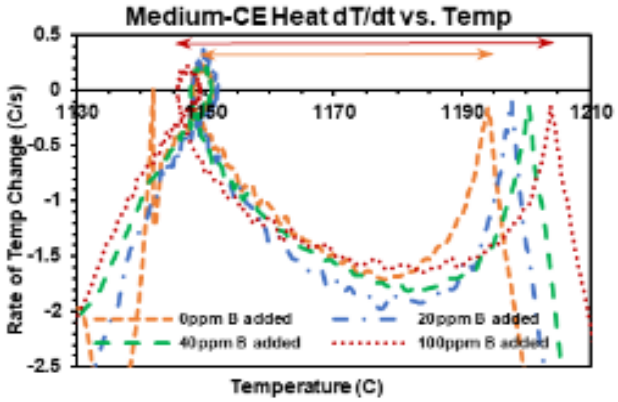

Figure 18. 1st derivative of the cooling curve plotted against temperature for medium-CE heat for the solidification. The difference between T_L and T_{Emin} is highlighted by arrows.

Table 8. The difference between the liquidus and eutectic minimum temperature for both the heats.

Heat	B-added, ppm	T_L (˚C)	T_{Emin} (˚C)	$T_L - T_{Emin}$
High-CE heat	No B-added	1157.3	1151.4	5.9
	20	1157.3	1149.7	7.6
	40	1158.4	1151.4	7
	100	1159.3	1150.3	9
Medium-CE heat	No B-added	1193.3	1147.5	45.8
	20	1195.8	1146.3	49.5
	40	1199.3	1146.7	52.6
	100	1202.2	1144.8	57.4

Observation and ImageJ quantitative analysis of the unetched microstructures for both heats were done to understand the B effect on graphite morphology (Figure 19). A measurement error of ±10% is considered for both the heats.

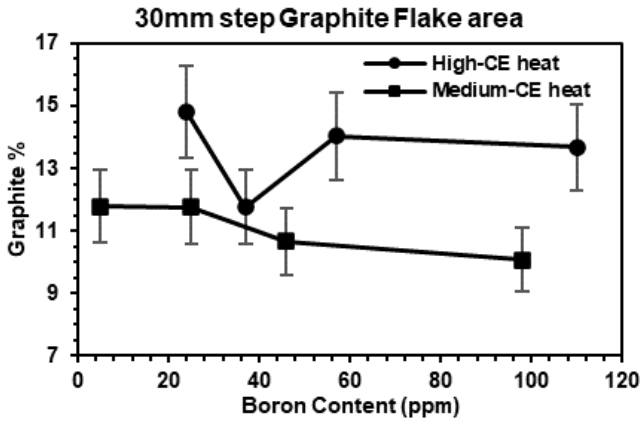

Figure 19. The area of graphite flakes for the 30mm step of the step block for both the heats.

4.2. EUTECTOID TRANSFORMATION

The first derivative of the cooling curve as a function of temperature for high-CE and medium-CE heats are shown in Figure 20 and Figure 21, respectively. Similar to the eutectic graph, the diameter of the loop is the eutectoid recalescence. The parameters V_{Trans} and T_{Trans} are obtained from these curves. The highest value of the first derivative of the cooling curve is called the velocity of transformation (V_{Trans}) whereas the temperature corresponding to this value is T_{Trans}. This data is tabulated in Table 9. In a previous work by Sertucha et.al [7], these parameters were used to predict the ferrite-pearlite formation. When ferrite content in the matrix decreases, and consequently the pearlite content increases, the solid-state transformations occur at lower temperatures and higher V_{trans}.

Hence, the eutectoid recalescence is higher during pearlite formation and lower for ferrite formation. In Table. 9 it is seen that both conditions are preferable for ferrite formations for the medium-CE heat with B additions above 20ppm. However, 20 ppm B addition increased the V_{Trans} in both heats, which is an indicator that small B additions can

affect the pearlite transformation. These results indicate that the effect of B on eutectoid reaction is not linear and depended on CE.

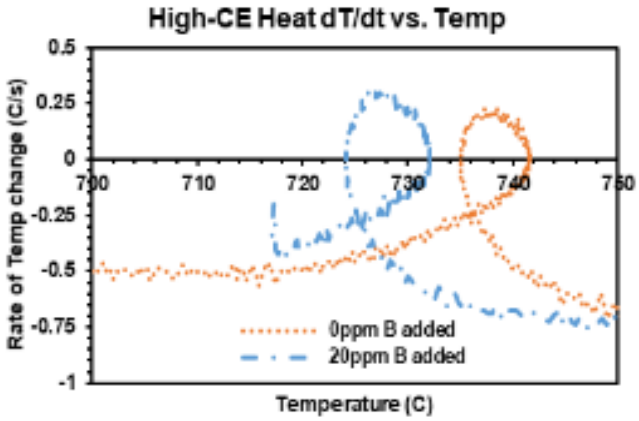

Figure 20. 1st derivative of the cooling curve plotted against temperature for high-CE heat for the eutectoid reaction.

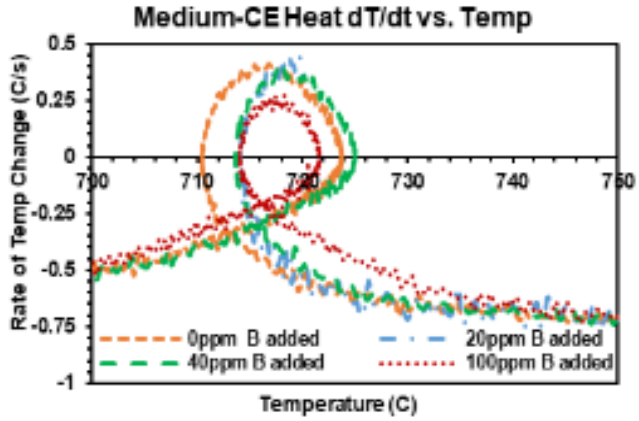

Figure 21. 1st derivative of the cooling curve plotted against temperature for medium-CE heat for the eutectoid reaction.

Table 9. Eutectoid parameters obtained from the cooling curve and the first derivative of the cooling curve of the eutectoid reaction.

Heat	B-added, ppm	Eutectoid Low (˚C)	V_{Trans}, C/s	T_{Trans} (˚C)
High-CE heat	No B-added	735	0.232	738.5
	20	724.1	0.315	726.4
	40	-	-	-
	100	-	-	-
Medium-CE heat	No B-added	710.5	0.411	716.8
	20	714.1	0.442	-
	40	713.6	0.386	717.7
	100	714	0.273	718.3

4.3. MICROSTRUCTURE ANALYSIS

The microstructural analysis of the specimens was used to validate the results obtained from the thermal analysis. The chill wedge analysis was done in order to understand the effect of B on carbide forming tendency. Images taken from the chill wedges of the high-CE and medium-CE heat are given in Figure 15 and Figure 16, respectively. For the high-CE heat, the chill tip was not visible to the naked eye, whereas, in the case of medium-CE heat, the chill tip was clearly visible. The chill depth for medium-CE heat increased with B additions. The chill depth measured is shown in the image. To check the carbide structures in high-CE heat, etched microstructures were taken at 5 areas, at the chill tip, and then at 5mm increments from the tip up to a distance of 20mm. The images were then arranged in a way to get a panoramic view of the chill wedge as seen in Figure 15. The same procedure was done for the medium-CE heat as well in Figure 16. As B increased in high-CE chill samples, carbide became visible in the chill tip. For the highest B samples, the carbides are seen up to 10mm from the chill tip. For the medium-CE specimens, the carbide precipitates are clearly visible and are seen further away from the

chill tip as the amount of B increases. Analysis of the smallest step, i.e., the 5mm step of the step block, was done as a supplement to the chill wedge analysis. The etched microstructures of the 5mm step are given in Figure 22 and Figure 23 for high-CE and medium-CE heats, respectively. It is clearly shown that there is carbide precipitation in the highest B sample of the medium-CE heat. The appearance of carbide is a clear indicator of the carbide stabilizing capabilities of B. The carbide promoting effect of B may be dependent on the cast iron CE because, at the same B level, no such carbide precipitation was shown in the high-CE heat.

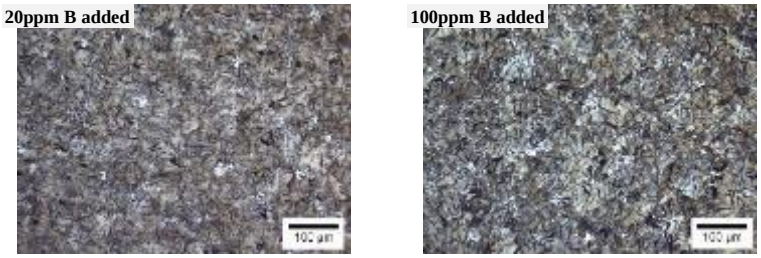

(a) (b)

Figure 22. Etched microstructures of the 5mm step of high-CE heat step block, (a) 20ppm B-added and (b) 100ppm B-added. There is no visible carbide precipitation.

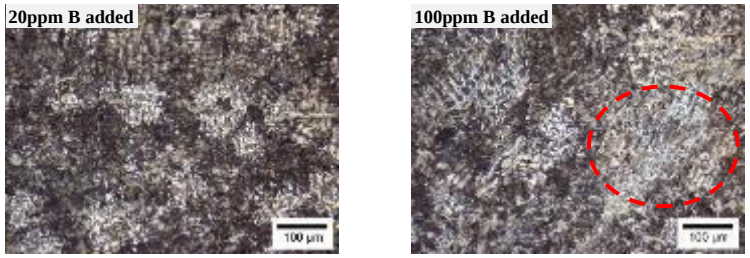

(a) (b)

Figure 23. Etched microstructures of the 5mm step of medium-CE heat step block, (a) 20ppm B-added and (b) 100ppm B-added. Carbide precipitation is visible in the highest B sample highlighted by a dashed circle.

The microstructures obtained from the 30mm step of the step block were used to evaluate ferrite forming tendency. In the high-CE heat (Figure 7) the microstructure of the matrix mainly consists of pearlite along with a considerable amount of ferrite enveloping the graphite for all B additions. These specimens had higher amounts of ferrite because of the well-known ferrite stabilizing effect of Si. The microstructures from the 30mm step of the step block of the medium-CE heat are had a mainly pearlitic matrix, with very minor areas of ferrite surrounding the graphite (Figure 9). Using ImageJ for quantification of the ferrite area of images in Figure 7 and Figure 9, the graph in Figure 24 was generated. From the graph, it is shown that the ferrite content for high-CE heat increases with the exception of the specimen without boron (Image 1A in Figure 7). The same effect can be observed for the medium-CE heat, however, the increase in ferrite is very low as compared to high-CE heat. This trend is also observed in the 20mm step as well as the 10mm step. The change in the intensity of the effect of B addition is notable. This effect is more profound in the high-CE heat than that in the medium-CE heat. This is additional proof that the B effect is dependent on CE.

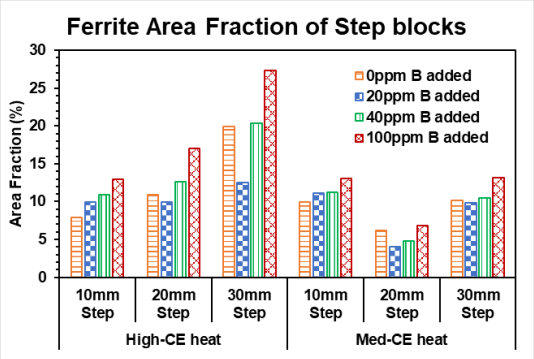

Figure 24. The ferrite area coverage as measured by optical metallography of the step block casting for medium and high CE heats.

4.4. MECHANICAL PROPERTIES

The tensile data are given in Table. 6 for both the heats. In the high-CE heat, the tensile strength increases for the 20 ppm B addition, but then it tends to reduce for higher B additions. In the medium-CE heat, a clear trend of increasing UTS with increasing B content (Figure 25) is observed. A one-way ANOVA analysis and Fisher's Criterion analysis were used for statistical evaluation of these differences at an 80% confidence level. The boxplot and Fisher analysis graphs are plotted for high-CE heat in Figure 26 and Figure 27, respectively. Similarly, a boxplot and Fisher analysis graphs are plotted for the medium-CE heat in Figure 28 and Figure 29, respectively. Based on the results from the statistical analysis, the data is statistically significant with 80% confidence with few exceptions. The hardness specimens were taken from the step block in the area closest to the central plane of the casting (Figure1). The data for both the heats is given in Table. 7. Hardness increased with tensile strength.

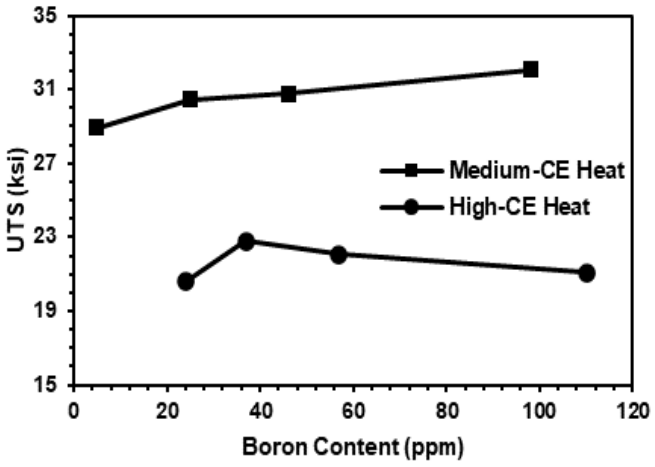

Figure 25. Comparison of UTS as a function of boron for both CE heats.

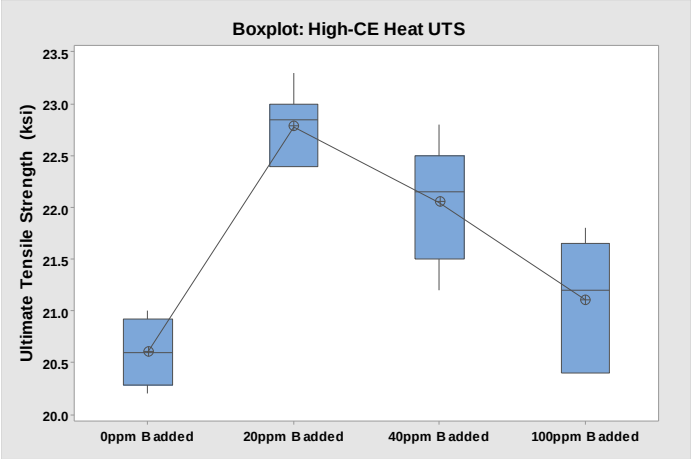

Figure 26. Boxplot showing the variation in UTS as a function of boron for the high-CE heat.

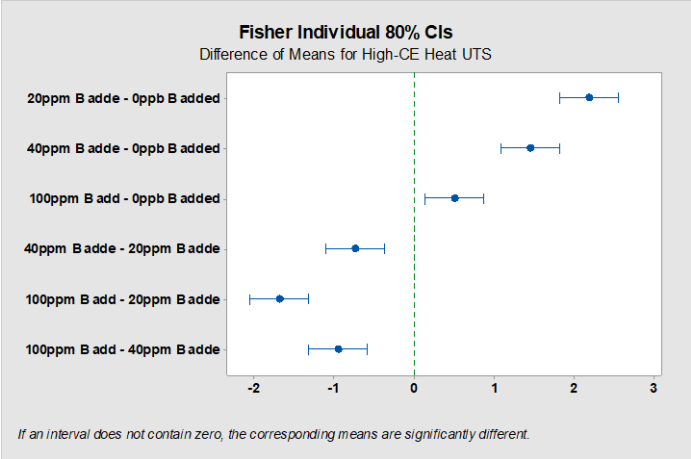

Figure 27. Fisher's analysis of UTS statistical significance as a function of boron for high-CE heat. The top three pairs of test results are significantly different at an 80% confidential level.

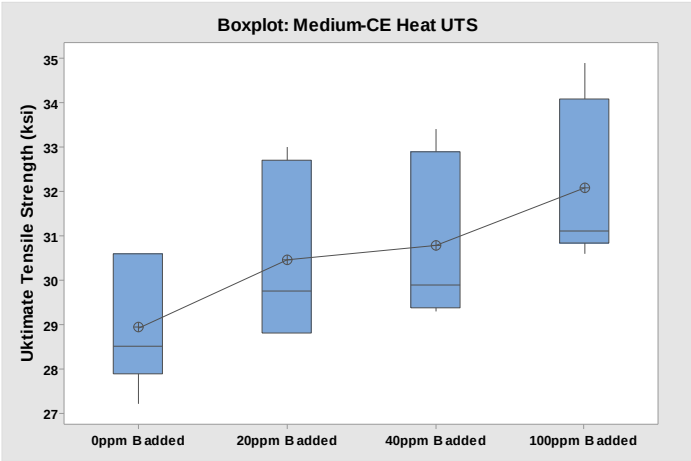

Figure 28. Boxplot showing the variation in UTS as a function of boron for the medium-CE heat.

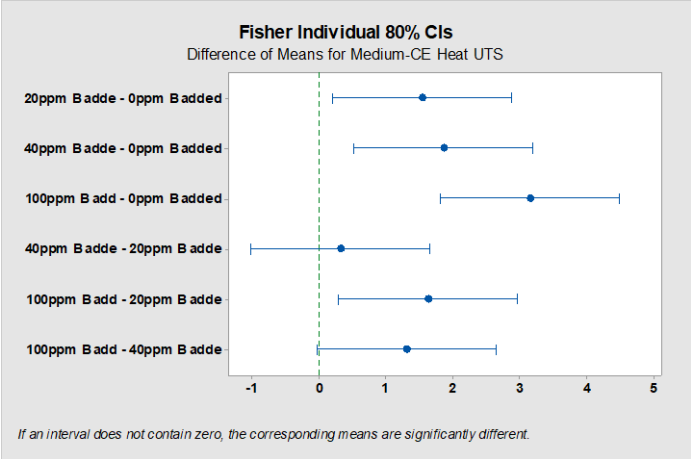

Figure 29. Fisher's analysis of UTS for medium-CE heat as a function of boron content. The results show that UTS is significantly different at an 80% confidence level, except for pairs of 40-20 B ppm and 100-40 B ppm.

5. CONCLUSION

The effects of boron on the microstructure and mechanical properties of gray iron were studied in two heats with high and medium carbon equivalents, CE, related to ASTM A48 Class 30B cast irons. Thermal analysis of the solidification and solid-state cooling curves showed that boron acts as an austenite stabilizer and affects the nucleation of graphite by changing undercooling during the eutectic reaction. The carbide forming tendency of large boron additions was confirmed by a metallographic study of chill wedge depth and step block castings. During the eutectoid reaction, the thermal analysis showed that the effect of boron on the ferrite/pearlite transformation is significant. Boron acts as a ferrite stabilizer when present in high amounts (above 35ppm). However, the effect of low boron additions (less than 20 ppm) was not understood clearly. The microstructural analysis of the heats replicated the results predicted from the thermal analysis, although the intensity of the effect was different for both the heats, suggesting the effect of boron is dependent on CE. More studies will be performed in the future to uncover the mechanisms for the ferrite stabilizing effect of boron. The effect of boron on the mechanical properties of gray iron might also be influenced by the CE of cast iron. In the high-CE heat, tensile strength increased only with 20 ppm boron addition, however, boron additions increased the tensile strength consistently in the medium CE heat. Future work will include a study of boron addition in low CE cast iron, class 40.

ACKNOWLEDGEMENT

The authors of this paper greatly acknowledge the contributions of the Undergraduate and Graduate research students at the Missouri University of Science and Technology for their assistance and guidance in the progress of this research. The authors would also like to extend their gratitude to the Foundry partners and the Steering Committee for their continuous support and direction throughout the project.

REFERENCES

[1] K. Ankamma, “Effect of Trace Elements (B and Lead) on the Properties of Gray Cast Iron,” J. Inst. Eng. India Ser. D (January-June 2014) Vol. 95 Issue (1), pp. 19-26. DOI 10.1007/s40033-013-0031-3.

[2] Robert Voigt, “ Trace (Minor) Elements in Cast Irons ”, ASM Handbook, Volume 1A, Cast Iron Science and Technology (2017)

[3] Sorel metal article: http://www.sorelmetal.com/en/publi/PDF/108_(2006).pdf

[4] Elimination and Neutralization of B in Ductile Irons by. R. L. Naro – ASI International, Ltd., Cleveland, Ohio. J. F. Wallace and Yulong Zhu – Case Western

[5] Doru M. Stefanescu, “ Trace (Minor) Elements in Cast Irons ”, ASM Handbook, Volume 1A, Cast Iron Science and Technology (2017)

[6] Alexander I Krynitsky, Harry Stern “Effect of B in structure and Some Physical Properties of Plain Cast Iron”, Research of National Bureau of Standards, Vol 42 (1949)

[7] J. Sertucha, R. Suárez, J. Izaga, L. A. Hurtado & J. Legazpi (2006) Prediction of solid-state structure based on eutectic and eutectoid transformation parameters in spheroidal graphite irons, International Journal of Cast Metals Research, 19:6, 315-322, DOI: 10.1179/136404606X167114

[8] Doru Michael Stefanescu, Ramon Suarez and Sung Bin Kim, “90 years of thermal analysis as a control tool in the melting of cast iron”, Special review, Vol 17, No 2, (2020)

[9] ASTM International. A48/A48M-03(2016) Standard Specification for Gray Iron Castings. West Conshohocken, PA; ASTM International, 2016. DOI: https://doi-org.libproxy.mst.edu/10.1520/A0048_A0048M-03R16

[10] ASTM International. E10-18 Standard Test Method for Brinell Hardness of Metallic Materials. West Conshohocken, PA; ASTM International, 2018. DOI: https://doi-org.libproxy.mst.edu/10.1520/E0010-18

II. MUTUAL B, TI, N EFFECTS ON PHASE TRANSFORMATIONS IN CAST IRON: THERMODYNAMIC CONSIDERATION AND EXPERIMENTAL VERIFICATION

S. Pawaskar, L.N. Bartlett, S. Lekakh

Department of Material Science and Engineering, Missouri University of Science and Technology, Rolla, MO 65409

Keywords: cast iron, boron, structure, thermal analysis, thermodynamic simulation

ABSTRACT

Even ppm levels of active elements such as Boron (B), Titanium (Ti), Nitrogen (N), and their combinations could significantly affect the microstructure and properties of cast iron, therefore understanding its mutual effect on phase transformations is important for industrial practice. To understand these mutual effects, a thermodynamic simulation of competitive B and TiN precipitates formation during solidification and cooling of gray cast iron with various levels of B was studied. The concept of "free iron borides (Fe-B)" in solid solution was suggested for controlling ferrite in the matrix. The hypothesized results from the thermodynamic study of B, N, and Ti added chemistries were evaluated in an experimental laboratory heat.

1. INTRODUCTION

Good casting capabilities, sound mechanical and physical properties, simplicity in production, and the low cost makes cast iron very versatile in a variety of industrial applications over centuries. Although most of these mechanical properties are affected by the chemical content of elements like C, Si, Mn, and Cr the trace elements in cast iron also have their fair share of contributions towards enhancing or deteriorating the properties of the casting. One of these trace elements which has been causing some sporadic problems for the iron foundries is B.

During the last decade, the addition of B to automotive-grade steel has increased. The hardenability provided by B has found many applications in the automotive panel class steels. This B-added steel then finds its way through scraps into the cast iron charges. Complaints have been received from the gray iron foundries about intended quality control issues with such B-added material. Another source of B in gray iron can be the fresh furnace linings.

The effect of B as a strong carbide stabilizer was studied by Ankamma et.al [1] wherein the presence of B above 550ppm proved disastrous to the iron in terms of chill and cracking problems in thin section castings. It can also cause the formation of undesired graphite flake structures like type D and reduce the strength of the material. Smaller graphite structures like type D can cause very fast carbon diffusion from the matrix to graphite flakes creating regions of ferrite that can adversely affect the mechanical properties of gray iron. In a study conducted by Alexander et.al [2], increasing B content

was seen to reduce the temperature gap between liquidus and solidus temperatures and increase the undercooling effects.

Another effect of B is seen to be that it is a ferrite stabilizer [3] as well. Its presence can cause severe effects on pearlitic-grade gray iron. B may counteract with the pearlite stabilizing elements like Cu, and Mn resulting in 'soft' pearlitic castings. The study performed previously on Class-30 gray iron [4] gave proof of B acting as a ferrite promoter and a carbide stabilizer. The ferrite promoting effect of B was studied with the help of eutectoid transformation analysis. Since B was the only varied element in that study, the synergistic effect of B with other alloying elements is not yet understood.

Ti is one of the common impurities in cast iron and steel. The use of Ti to pin N in B-added steels and improve the formability is a common practice in steel making. N helps pin down the B in these steels and reduces the hardenability provided by B [5]. Using the same principle, the combined effect of B, N, and Ti was studied in this investigation.

The purpose of this investigation is to provide experimental information on the synergistic effect of B, N, and Ti on the properties of Class-30 gray iron. This article includes the use of thermodynamic simulation to predict the B interaction with the gray iron phases in presence of N and Ti. The concept of 'Free iron borides' i.e., the B which is not pinned by N and thus reacted with the matrix is hypothesized to have an effect on the gray iron properties. The properties under investigation were phase transformation parameters obtained from the thermal analysis, microstructure, chilling tendency strength, and hardness.

2. METHODOLOGY

The experiment was performed in three phases. (i) phase I, simulation of the distribution of B in GI phases, (ii) phase II, predicting effects of N and Ti on B distribution, and (iii) experimental verification of the simulations in a foundry heat.

In phases I and II, a Class 30 GI simulation was performed using ThermoCalc software to understand the distribution of B in GI. Databases included B, Ti, and N solutions in liquid, austenite (γ), ferrite (δ), and different compounds (iron boride (Fe_2B) and nitrides). The chemistry of the simulated gray iron is given in Table 1. The level of B was varied from 5ppm to 98ppm to study the B distribution between phases at two specific temperature regions: near solidus (T_{Sol}) and the eutectoid transformation (A_3). The B distribution at the eutectoid transformation was studied at 3 points, just before the transformation A_3(+), just after the transformation A_3(-), and after the transformation was completed A_3(-)(-). The three points were selected to observe the B distribution in the transformed phases (austenite and ferrite). Then, the same base chemistry with fixed 100 ppm B was used, and N varied from 50ppm to 100ppm to 150ppm. After that, the simulations were performed with varying levels of Ti up to 0.05%.

In experimental phase III, a Class 30 GI heat was cast in the laboratory, with the same targeted chemistry as considered for the thermodynamic simulations (Table 1). Heats were performed in a 200lb induction furnace. The amount of B in the chemistry was fixed to 65ppm in the initial melt and for the second chemistry, 50ppm N was added using Nitrided Ferro-Manganese. For third chemistry, 0.020 wt.% Sn was added and for the last 0.050 wt.% Ti was added in form of Ferro-Titanium.

The charge for the heat consisted of high purity induction iron ingots, ferrosilicon, ferromanganese, metallic chromium high purity graphite, and foundry returns from our foundry sponsor. The argon flow rate, to protect the melt, was kept at 35 SCFH.

In order to check the CE in the melt, thermal analysis with tellurium (Te) added cups were used. The tapping temperature for the heat was maintained between 1400-1420°C. The metal was tapped into a 22lb hand ladle. Each chemistry required two hand ladles. The inoculation was done for each hand ladle during tapping by 0.3% commercial inoculant (70% Si, 0.17% Al, 0.76% Sr).

In order to record the chemical compositions, two types of samples were used: an immersion sampler and a Cu chill mold. To understand the effect of studied variables on the mechanical properties of gray iron, multiple molds were poured for each chemistry, including blocks with 5, 10, 20, and 30 mm steps (Figure 1), 6 ASTM B-bars, and chill wedges.

To perform a comparative study, data from a previous heat with varied B and 4.1 CE was used and denoted as Heat 1. Heat 1 was described in our publication4. The heat performed for this study, denoted as Heat 2, had variable chemistries as 2A (base B-added in induction furnace), 2B (+N added in ladle), 2C (+Sn added in ladle), and 2D (+Ti added in ladle).

Thermal analysis was performed by obtaining the cooling curves from thermal analysis software using non-Te cups (Figure 2a). The cooling curves were used to analyze the effects of additions on eutectic and eutectoid reactions. The nomenclature of used parameters and their variation at critical temperatures were studied as suggested [6],[7] and shown in Figure 2b.

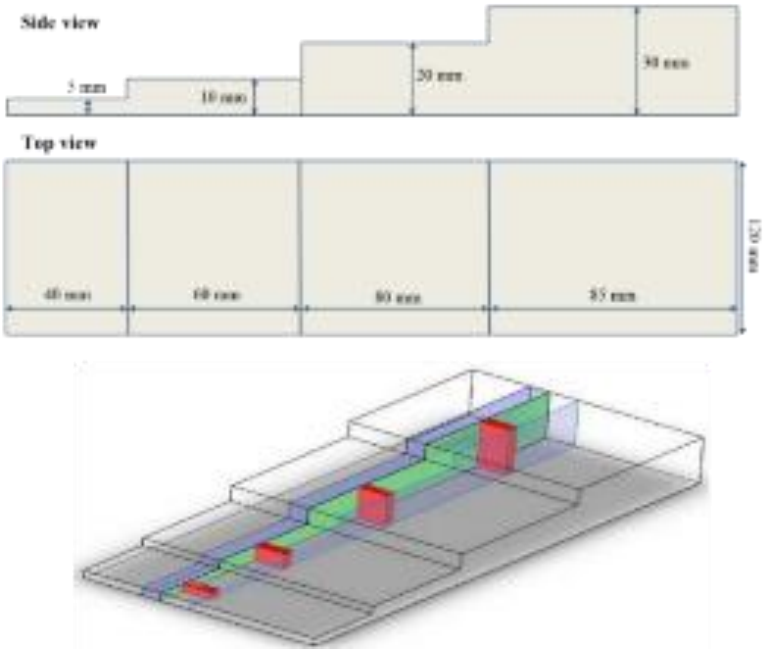

Figure 1. Side, top, and isometric view of step block. The red area was used for metallographic analysis and hardness was measured in the green section.

Table 1. Target Chemistries (wt.%) for the thermodynamic simulation and foundry heat.

Heat	Thermodynamic Simulation		Heat 2
Description	Phase I	Phase II	Phase III
C	3.45	3.45	3.40~3.45
Si	2.05	2.05	1.7~1.8#
CE	4.13	4.13	4.10~4.15
B (ppm)	5/25/48/98	100	65
Cr	0.21	0.21	0.17~0.21
Mn	0.58	0.58	0.50~0.55
N (ppm)	50	50/100/150	-
Ti	-	0/0.05	0.055
Sn	-	-	0.020
S (ppm)	50	50	-

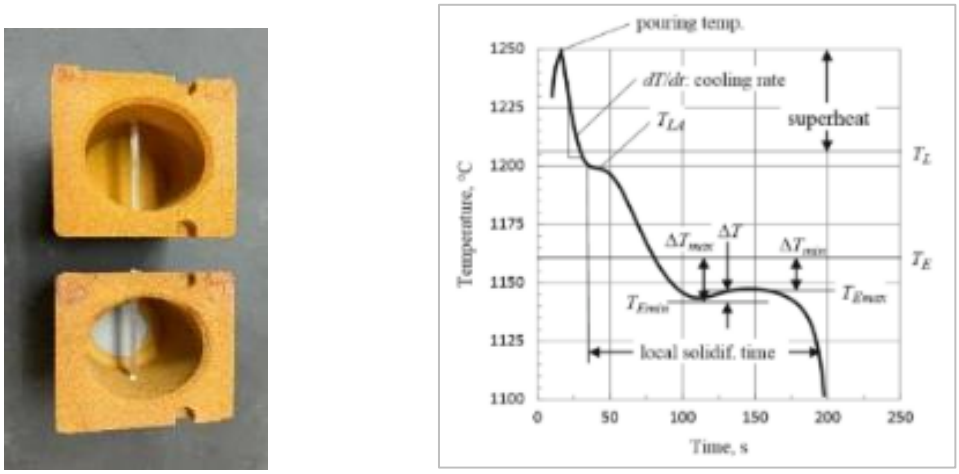

(a) (b)

Figure 2. (a) Images of the TA cups non-Te on the top and Te cup on the bottom, (b) Nomenclature of used parameters from thermal analysis software.

The chemical composition analysis was done using Optical Emission Arc Spectroscopy (OES) and C, S, N from combustion analysis using the commercial C, S, N, O analyzer. Four standards with 2, 30, 76, and 400 ppm B were used for calibration. Specimens for optical metallography were taken from the step blocks (red sections in Figure1). For quantifying the metal matrix, etched by 3% Nital images were analyzed using ImageJ software. Tensile tests were performed at 0.02mm/s strain rate on a 250kN hydraulic tensile frame in accordance with the ASTM A-48[8] for the B-type bar. Hardness tests were done in accordance with ASTM E10-18[9] with verification using certified hardness blocks.

3. RESULTS

3.1. SIMULATIONS

The results from ThermoCalc for B distribution in the base cast iron are shown in Table 2. At any given temperature, the sum of B in all the phases would be equal to the total B content of the studied alloy. The critical temperatures obtained from ThermoCalc were used to simulate distributions and these temperatures had some deviations from experimentally measured temperatures by thermal analysis, which could be a result of departure from equilibrium or small discrepancies in the used databases. The T_{Sol} in simulations means less than 5% liquid.

Four levels of B were used in phase 1 simulations (Table 2). At the solidus for the 5ppm B level, the majority of B was dissolved in the austenite and only 1ppm was spent to form Boron Nitride (BN). As the temperature reduces and approaches A_3, all B was tied up as BN. So, no residual B is seen to react with any other phases. Moving on to the 25ppm results: some B was seen in austenite at T_{Sol}, whereas a majority of it is tied up as BN. On approaching A_3, all the B from austenite reacted with N and formed BN, thus no free B. However, as the B concentration in alloy increases to 48ppm, the amount of B dissolved in austenite increases at T_{Sol}, up to 25ppm in solid solution. On approaching the A_3, the amount of BN reaches a maximum of 39ppm. This amount was limited by available N and the excess B then starts to form Fe_2B; a small portion (1ppm) is seen in ferrite. This could be considered a critical B concentration in cast iron. The excess B left after all BN is formed, will be called “Free B” in this article, which can be detrimental to cast iron. In the 98ppm B, the distribution pattern was similar to the 48ppm, at T_{Sol}, the amount of B in

austenite increased whereas the amount of BN formed was similar. As A_3 is reached, the amount of BN maxes out to 39ppm as in the previous chemistry and all the excess B is seen as “Free B”.

In these simulations, a typical 50ppm N level was considered, and this N level was required to pin a maximum of 39ppm of B in cast iron. These results were experimentally verified in the previous heat with variations of added B. Moreover, thermodynamic simulations could also predict the other B interaction with impurities which could be important for foundry practice when many types of impurities are present in the melt.

One of the practically important impurities is Ti because this element could also form nitride and compete with B. To study the possible Ti, B, and N interactions, the same chemistry with 100ppm B was used at the same CE. The amount of N was varied from 50 to 150 ppm and Ti was varied from 0 to 0.05 wt.%. The interaction results with excess N are given in Table 3. For the 50 ppm N chemistry, at TSol, the max B dissolved in austenite was 21 ppm, the max B in BN was 35 ppm, and the rest of the B was Fe2B. As A3 approached, the BN maxed out to 39 ppm, and the rest of B formed into Fe2B. These results are similar to those presented in Table 2.

However, when the concentration of N was increased to 100 ppm, the amount of B in austenite and Fe2B fell considerably due to an increase in BN content. So, in this case, more N is available for pinning B. Moreover, when the N was raised to 150 ppm, all the B was successfully tied up as BN.

Table 2. Distribution of B (in ppm) between phases from the thermodynamic simulation of varying amounts of B in 4.1 CE cast iron with 50ppm N.

		γ	BN	Fe_2B	C_{Gr}	δ
Chem A 5ppm	T_{sol}	4	1	-	-	-
	$A_3(+)$	0	5	-	0	-
	$A_3(-)$	-	5	-	0	0
	$A_3(-)(-)$	-	5	-	0	0
Chem B 25ppm	T_{sol}	7	18	-	-	-
	$A_3(+)$	0	25	-	0	-
	$A_3(-)$	-	25	-	0	0
	$A_3(-)(-)$	-	25	-	0	0
Chem C 48ppm	T_{sol}	15	33	0	-	-
	$A_3(+)$	3	38	7	0	-
	$A_3(-)$	-	39	8	0	1
	$A_3(-)(-)$	-	39	9	0	0
Chem D 98ppm	T_{sol}	21	35	42	-	-
	$A_3(+)$	3	38	57	0	-
	$A_3(-)$	-	39	58	0	1
	$A_3(-)(-)$	-	39	59	0	0

When Ti was included in the simulations, the obtained results drastically differed (Table 4). For example, in cast iron with 0.05% Ti at 50 ppm N, no BN was formed, and all the B was considered as “free B”. As A_3 approached, the situation did not change, all the B reacted to form only Fe_2B, thus clearly indicating that all the N in the system was used up as TiN. Increasing the N to 100 ppm for the same Ti, some BN started to form and the amount of Fe_2B reduced. The. Increasing the N to 150ppm (which is above equilibrium in the melt), did not show any major variations in the no Ti and 0.05Ti case suggesting that N is excess in the system to cause any significant changes. Important practical predictions followed from these simulations. The other impurities could have a unique effect on “free B” and these predictions were verified in experimental Heat 2.

Table 3. Distribution of B in phases (in ppm) from the thermodynamic simulation of varying N in cast iron with 100ppm B.

N		γ	BN	Fe_2B	C_{Gr}	δ
50	T_{sol}	21	35	44	-	-
	$A_3(+)$	3	38	59	0	-
	$A_3(-)$	-	39	60	0	1
	$A_3(-)(-)$	-	39	61	0	0
100	T_{sol}	21	74	5	-	-
	$A_3(+)$	3	77	20	0	-
	$A_3(-)$	-	77	22	0	1
	$A_3(-)(-)$	-	77	23	0	0
150	T_{sol}	6	94	-	-	-
	$A_3(+)$	0	100	-	0	-
	$A_3(-)$	-	100	-	0	0
	$A_3(-)(-)$	-	100	-	0	0

Table 4. Distribution of B in phases (in ppm) from the thermodynamic simulation at varying N in cast iron with 100 ppm B and 0.05 wt.% Ti.

N		γ	BN	Fe_2B	C_{Gr}	δ
50	T_{sol}	21	-	79	-	-
	$A_3(+)$	3	-	97	0	-
	$A_3(-)$	-	-	99	0	1
	$A_3(-)(-)$	-	-	100	0	0
100	T_{sol}	21	71	8	-	-
	$A_3(+)$	3	71	26	0	-
	$A_3(-)$	-	71	28	0	1
	$A_3(-)(-)$	-	71	29	0	0
150	T_{sol}	7	93	-	-	-
	$A_3(+)$	0	100	-	0	-
	$A_3(-)$	-	100	-	0	0
	$A_3(-)(-)$	-	100	-	0	0

3.2. EXPERIMENTAL

The chemical compositions of the heats obtained from the OES are given in Table 5. The actual chemistry of Heat 2 was close to the target chemistry with small variations related to ladle addition recovery. Added to the induction furnace, B was similar in all ladles (62, 60, 65, and 70 ppm). Ladle B had elevated N, while Sn was added in Ladle C and Ti in Ladle D. The bottom row in this Table also provided information about previous Heat 1 with variation in B.

Table 5. Chemical composition for the Heat 2 and Heat 1 (presented in our previous publication), in wt.%

Ladle	Chemistry	C*	Si	CE	B (ppm)	Cr	Mn	P	S*	N* (ppm)	Sn	Ti
Target		3.40 ~3.45	1.7 ~1.8#	4.10 ~4.15	65	0.17 ~0.21	0.50 ~0.55	-	-	-	0.020	0.050
Induction Furnace		3.30	1.88	3.93	3	0.19	0.49	0.047	0.038	37	0.009	0.003
Ladle-A	Base	3.25	2.17	3.97	62	0.19	0.56	0.044	0.034	46	0.009	0.004
Ladle-B	+N	3.32	2.14	4.03	60	0.18	0.62	0.044	0.035	55	0.009	0.003
Ladle-C	+Sn	3.33	2.16	4.05	65	0.19	0.58	0.045	0.036	40	0.022	0.003
Ladle-D	+Ti	3.25	2.18	3.98	70	0.19	0.58	0.047	0.039	43	0.010	0.055
Heat 1 (variation in B)		3.45	2.05	4.13	5/25 /46/98	0.21	0.58	0.025	0.018	50	0.008	0.033

* C, S and N readings taken from commercial C, S, N, O analyzer. # Si target before inoculation

The thermal analysis parameters obtained from thermal analysis software using the non-Te cup in new Heats 2 and previous Heat 1 are shown in Table 6. It can be clearly seen from the data in Heat 2 that micro-alloyed additions N, Sn, and Ti had a minor effect on T_L in presence of 65ppm B; however, B itself significantly increased T_L in Heat 2 without the other impurities. On the contrary, the eutectic start temperature varied with micro-alloying additions in Heat 2. The eutectic start temperature reduces for the +N chemistry

in Ladle B, whereas it increases for the Ti addition in Ladle D vs the base Ladle A without additions at the same 65ppm B level in all cases. In Heat 1 without these impurities, the increase in eutectic start temperature was directly related to the B content. The solidification cooling curves for these two heats are shown in Figure 3.

Table 6. Thermal analysis data obtained from thermal analysis software for both the heats.

Heat	Heat 2 (N, Sn, Ti additions in B-alloyed)				Heat 1 (B variation)	
Chemistry	Ladle A (base 65 ppm B)	Ladle B (+N)	Ladle C (+Sn)	Ladle D (+Ti)	Base (5 ppm B)	100 ppm B-added
Liquidus Temp, T_L (˚C)	1207.7	1203.7	1205.1	1210.4	1193.3	1202.2
Eutectic Start, T_{EStart} (˚C)	1185.8	1182.7	1184.2	1188.3	1176.9	1180.9
Eutectic Minimum, T_{Emin} (˚C)	1148.8	1146.9	1149.1	1148.3	1147.5	1144.8
Eutectic Maximum, T_{Emax} (˚C)	1151.3	1150.2	1152.1	1151.2	1150.5	1148.2
Solidus Temp (˚C)	1107.3	1108	1109.8	1106.3	1100.8	1107
Recalescence, ΔT (˚C)	2.4	3.2	3.0	2.9	3.0	3.4
Graphite Factor 1	64	69	69	61	72	71
Graphite Factor 2	32	27	29	37	24	35

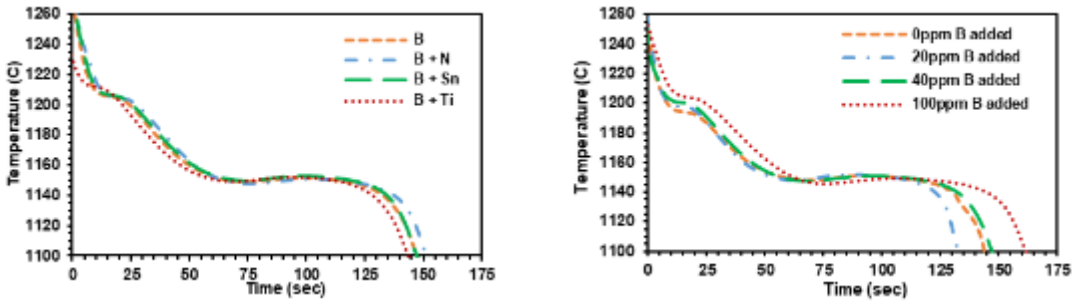

(a) (b)

Figure 3. Solidification cooling curve for (a) Heat 2, the N, Sn, and Ti micro-alloyed B-added heat, and (b) Heat 1, the variable B-added heat.

The cooling curves shown in Figure 4 represent the eutectoid reactions for two experimental heats. The red-dotted line represents the V_{Trans} for the eutectoid reactions. Eutectoid parameters like temperatures of eutectoid low and eutectoid recalescence were analyzed to understand the effect of B in solid-state transformation reactions. In addition, the 1st derivative of the cooling curve was plotted against the temperature for the eutectic and eutectoid reactions to analyze the change in cooling rates related to the latent heat liberation and the Eutectoid parameters like V_{Trans}. This data analysis is presented in the Discussion part of this article.

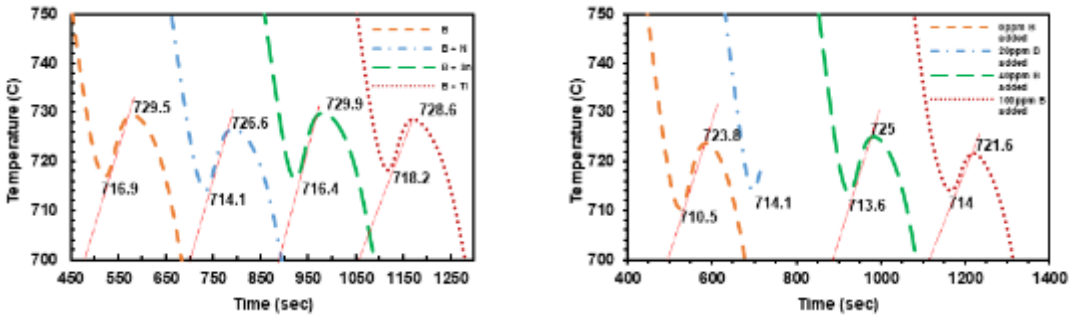

(a) (b)

Figure 4. Eutectoid cooling curve for (a) Heat 2, the N, Sn, and Ti micro-alloyed B-added heat, and (b) Heat 1, the variable B-added heat.

The unetched and etched microstructures obtained from the 30mm and 20 mm sections of step blocks from micro-alloyed Heat 2 are shown in Figure 5 and Figure 6. In the 30mm section, a lower ferrite area is seen in N and Sn added cast irons from Ladle B and Ladle C when compared to the base Ladle A at the same boron level. On the contrary, Ti-added ladle D showed higher ferrite content. Similar behavior was seen in the 20 mm

section also. Analysis of the microstructure images from the smaller steps i.e., 5mm and 10mm of both the heats was also done, but since the matrixes in the 5mm and 10mm steps were majorly pearlite no specific differences were seen in those images.

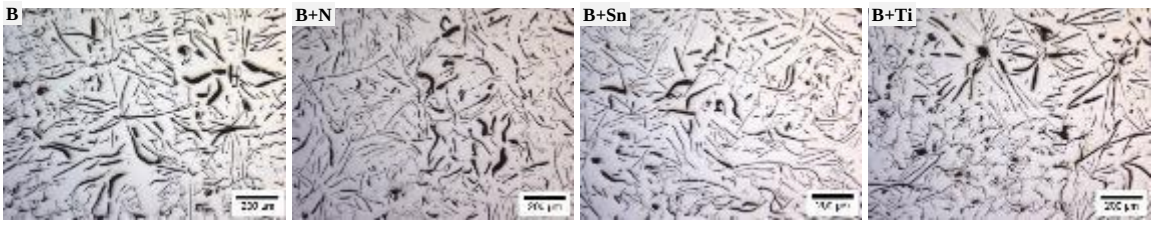

(a)

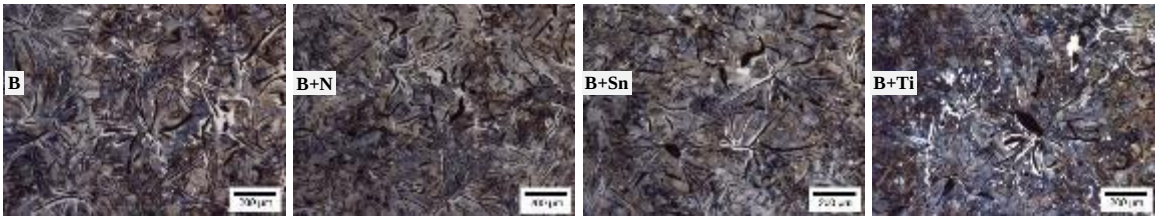

(b)

Figure 5. Unetched (a) and etched (b) microstructures taken from the 30mm section of cast step block from Heat 2 with different micro-alloy additions listed in Table 2.

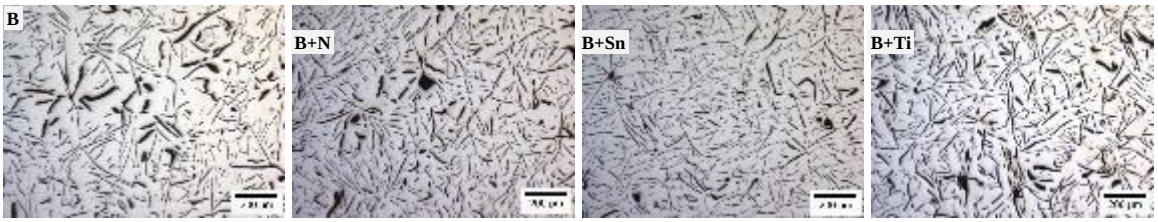

(a)

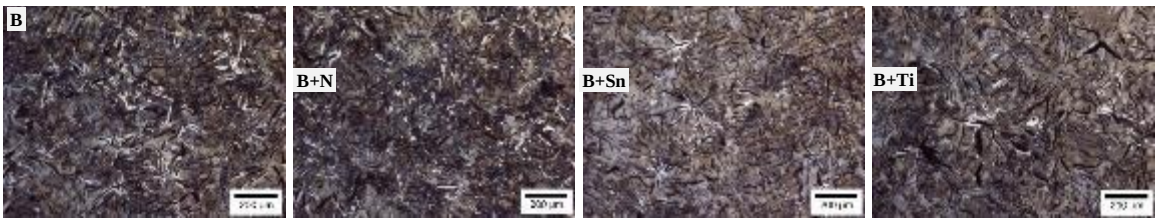

(b)

Figure 6. Unetched (a) and etched (b) microstructures taken from the 20mm section of cast step block from Heat 2 with different micro-alloy additions listed in Table 2.

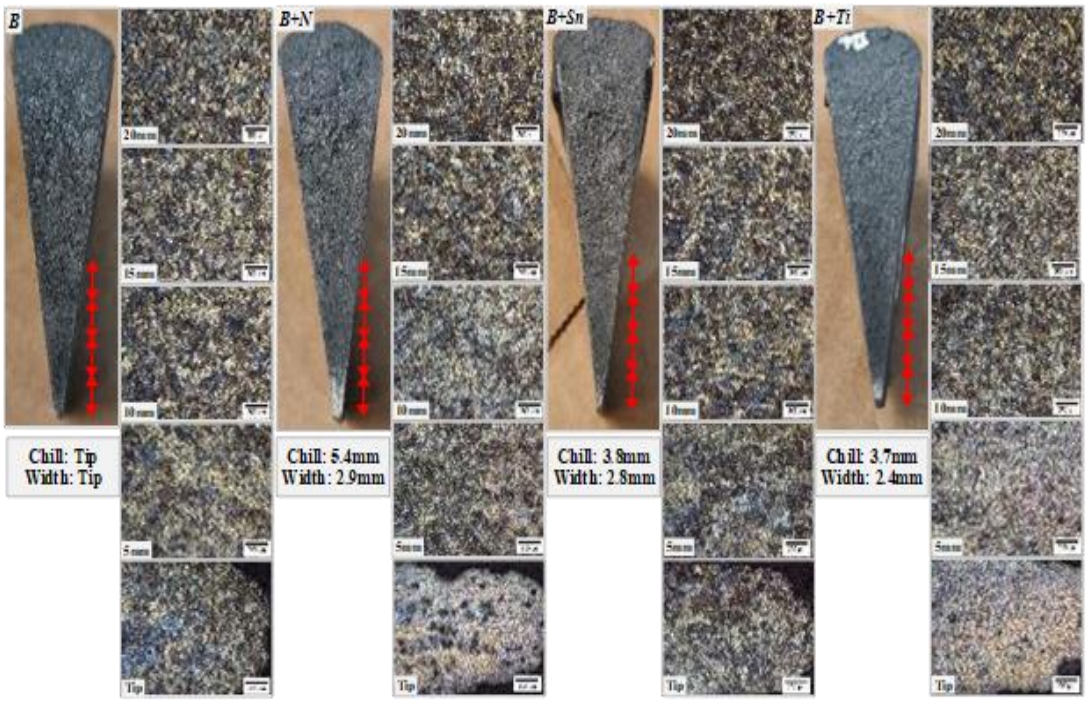

Figure 7. Chill wedge fractures and etched microstructures taken at the chill tip and regions at 5mm increments up to 20mm from the micro-alloyed Heat 2 with different additions from left to right: base, +N, +Sn, and +Ti.

4. DISCUSSION

4.1. THERMODYNAMIC SIMULATIONS

Accordingly thermodynamic simulations, there was no indication of the existence of BN precipitate in the melt at studied concentrations. However, it was predicted that N starts reacting with the B when the solidus temperature was reached. Although in cases with higher B (above 48ppm) not all the B reacted to from BN at the typical 50 ppm N level indicating that some B is retained in austenite solution until A_3 is reached. As the amount of B increased, the BN formed also increased until all the N is used up and the

excess of B then reacts to form a relatively weak intermetallic compound Fe_2B. We suggested calling this “free boron” when compared to strongly tied B in nitride.

By varying the amount of N and B in the chemistry, it is possible to define boundary conditions for “free B” and was it seen that N is the limiting factor for the interaction of B. Also, it showed the other possible route which could increase the amount of ”free B”, by Ti addition. This addition can be used to tie N in form TiN which resulted in an increase in the formation of “free B”. The amount of Ti was limited to 0.05% in the simulations so the effect of Ti to pin N was seen at 50 ppm N only. Increased levels of N like 100 ppm (which could be possible with N-bearing ferroalloys or during cupola or EAF melting) and 150 ppm (with is only hypothetical and not practically realistic) would need more Ti to prevent BN formation.

Figure 8 illustrates the joint mutual effect of B, N, and Ti by presenting fields where strong nitride or weak intermetallic borate will be presented. The red region in the graph is the critical region experimentally tested in this study. Any increase in N can push this region towards the right, i.e., increased effective N and more BN formed. The addition of Ti shifts the Fe_2B/BN boundary line down, due to lesser available N i.e., more effective B content and increased Fe_2B formation. In terms of the working hypothesis, which assumed that “free B” promotes ferrite formation during austenite decomposition, these impurities could provide different effects on the metal matrix structure: N could suppress while Ti will promote ferrite formation

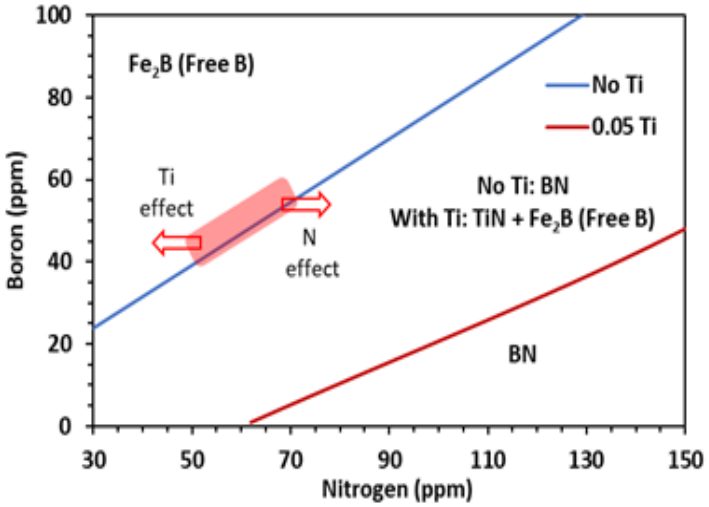

Figure 8. Representative graph indicating the effect of N and Ti for a given B content.

4.2. SOLIDIFICATION

The cast iron chemistry was hypo-eutectic and its solidification started with primary austenite. The plot of the 1st derivative curve of the eutectic cooling curve against Temperature for the Heat 1 (B addition in pure cast iron) and Heat 2 (B with micro-alloying additions) is given in Figure 9. The rightmost peak in the graph marks the austenite nucleation. The leftmost point of the loop is the eutectic low temperature T_{Emin}, while the rightmost point of the loop is the eutectic high, T_{Emax}. The diameter of the loop will give the eutectic recalescence.

The effect of B on the T_L is seen clearly in Table. 6. In comparison with the Base B chemistry, the B+N chemistry had lower T_L, whereas the B+Ti had a higher value, similar to the Heat 1 high B chemistry. From the graph, it can be seen that the austenite nucleation is affected significantly in both heats. In unalloyed Heat 1, B additions promoted austenite precipitation similar to the combined B+Ti additions in Heat 2. It could be

contributed to the nucleation effect of tiny nitrides developed in the melt. While thermodynamic equilibrium did not predict such precipitates above the liquidus temperature, transient conditions of addition dissolution in the melt and segregation during austenite solidification could promote nitride formation.

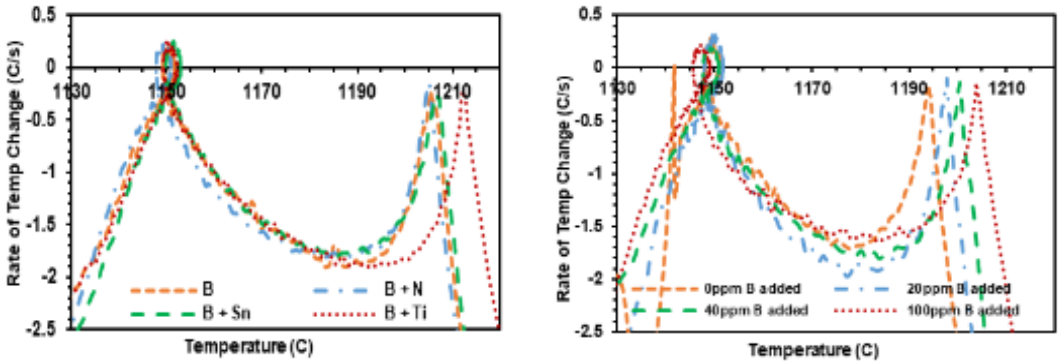

(a) (b)

Figure 9. 1st derivative of the cooling curve in solidification region plotted against temperature for (a) Heat 2, the N, Sn, and Ti micro-alloyed B-added heat, and (b) Heat 1, the variable B-added heat.

B in the heat 1 and the other studied micro-alloy additions in the heat 2 provided detectable effects on the eutectic solidification. In heat 1, high B lowered T_{Emin} and T_{Sol} (Figure 3b and Table 6) indicating a chilling tendency. In the B-added heat 2, N also decreased T_{Sol} (Figure 3a and Table 6). This could be related segregation effect of these impurities in the last portion of solidified eutectic at the grain boundary. Together with decreasing temperature such segregation could promote a local chilling effect.

4.3. EUTECTOID TRANSFORMATION

1st derivative vs temperature for complex micro-alloyed Heat 2 and pure with B additions Heat 1 are shown in Figure 10. Like on the eutectic graph, the diameter of the loop in Figure 10 is the eutectoid recalescence. The parameters V_{Trans} and T_{Trans} were obtained from these curves. The highest value of the 1st derivative is called the velocity of transformation (V_{Trans}) whereas the temperature corresponding to this value is T_{Trans}. The details about these eutectoid parameters, their notations in the graphs, and predicted effects are given in Table 7. These parameters which were obtained from Figure 10 for both the heats are tabulated in Table 8. In a previous work by Sertucha et.al [7], these parameters were used to predict the ferrite-pearlite formation. Hence, the eutectoid recalescence is higher during pearlite formation and lower for ferrite formation, when the solid-state transformations occur at lower temperatures at higher V_{Trans}, ferrite content in the matrix decreases, and consequently the pearlite content increases. It is seen in Table. 8 that both conditions are fulfilled for the B+N addition in heat 2 as well as a high B level in heat 1. These changes in cooling curves suggest higher pearlite formation. On the other hand, the lower recalescence and V_{Trans} value and a higher T_{Trans} value in B+Ti chemistry in heat 2 suggest higher ferrite formation. Thus, the addition of N suppressed the ferrite promoting effects of B whereas Ti can enhance the ferrite promotion effect of B. Such effect was predicted from thermodynamic simulation applying the “free B” hypothesis. It must also be noted that the addition of Sn, which is a very strong pearlite stabilizer, has a very high recalescence and V_{Trans} value.

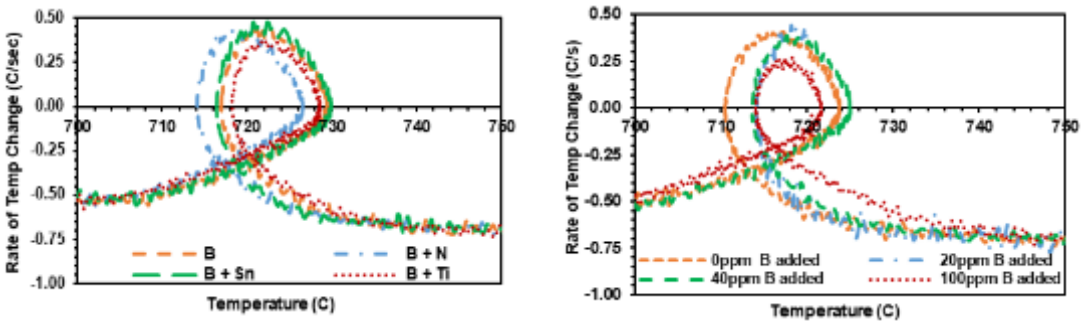

(a) (b)

Figure 10. 1st derivative of the cooling curve during the eutectoid reaction plotted against temperature for (a) Heat 2, the N, Sn, and Ti micro-alloyed B-added heat, and (b) Heat 1, the variable B-added heat.

Table 7. Eutectoid parameters notations and effects.

Eutectoid Parameter	DTA notations	Change	Effect
Eutectoid Low, T_{EuLow}	Left side of the loop	↑	Ferrite promotion
$\Delta R = T_{EuHigh} - T_{EuLow}$	Diameter of the loop	↓	Ferrite promotion
V_{Trans}, C/s	Highest point of the loop	↓	Ferrite promotion
Transformation Temp, T_{Trans}	Temp at the V_{Trans} value	↑	Ferrite promotion

Table 8. Eutectoid parameters obtained from the cooling curve and 1st derivative graphs of the alloyed B heat eutectoid reaction.

Heat	Chemistry	T_{EuLow} °C	ΔR	V_{Trans}, C/s	T_{Trans} °C
Heat 2 CE 4.0	B	716.9	12.6	0.439	721.3
	B + N	714.1	12.5	0.443	718.7
	B + Sn	716.4	13.5	0.476	720.9
	B + Ti	718.2	10.4	0.374	722.4
Heat 1 CE 4.1	No B-added	710.5	13.3	0.411	716.8
	100ppm B-added	714	7.6	0.273	718.3

4.4. MICROSTRUCTURE ANALYSIS

The microstructural analysis of the specimens was used to validate the results obtained from the thermal analysis and thermodynamic predictions. The microstructures obtained from the 30 mm step of the step block were used to evaluate ferrite forming tendency. In the 30 mm and 20 mm steps, microstructure (Figure 5 and Figure 6) the metal matrix mainly consists of pearlite along with some areas of ferrite content enveloping the graphite for all chemistries. Using ImageJ for quantification of the ferrite area of these images, the ferrite area was plotted in Figure 11. It is seen that the ferrite area fraction reduces with N addition in Heat 2 with 60-65 ppm B This effect was forecasted from thermodynamic simulations which predicted the mitigation effect of N on “Free B”. Whereas, with Ti addition, the ferrite area fraction increases, suggesting the enhanced B effect due to Ti because of competition to N.

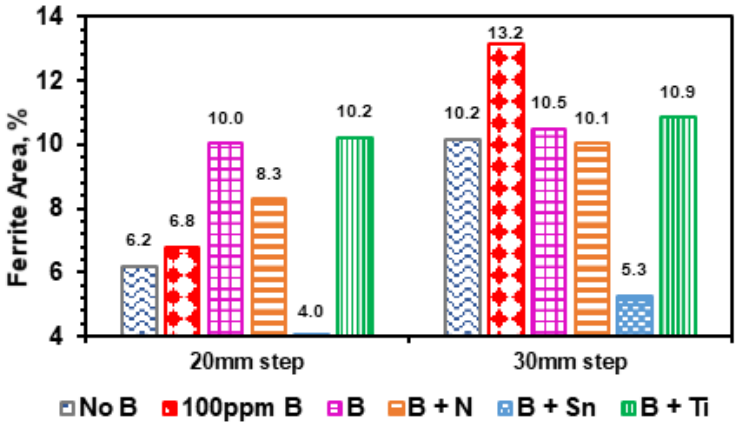

Figure 11. The ferrite area coverage as measured by optical metallography of the step block casting for both the heats.

5. CONCLUSION

The mutual effects of B, N, and Ti micro-additions were studied with the help of thermodynamic simulations and experimental methods including advanced thermal analysis. For the first time, the “free B” concept was suggested to link ferrite promotion in B-contaminated cast iron. This hypothesis was simulated for different B additions as well as it predicted the mutual effect of other impurities in cast iron. The thermodynamic simulations showed that elevated N can be used to tie down B and avoid B interacting with the metal matrix during the eutectoid reaction. On the other side, a common impurity such as Ti could compete for N and increase “free B”, promoting ferrite formation. It is important to note, that the suggested methodology was used for quantitative predictions of critical concentrations of multiple impurities. The experimental heat confirmed the theoretical thermodynamic predictions.

To conclude, the suggested methodology opened a new avenue for cast iron process optimization and could be directly used in foundry operations.

6. FUTURE WORK

Future work towards this research will include a study of B-added specimens to understand the places where the BN segregates in the matrix with low atomic weight characterization methods like TEM or wavelength dispersive spectroscopy.

ACKNOWLEDGEMENT

This investigation was funded by the American Foundry Society. The authors of this paper greatly acknowledge the contributions of the Undergraduate and Graduate research students and staff at the Missouri University of Science and Technology for their assistance and guidance towards the progress of this research. The authors would also like to extend their gratitude to the Foundry partners and the Cast iron research Steering Committee for their continuous support and direction throughout the project.

REFERENCES

[1] K. Ankamma, “Effect of Trace Elements (B and Lead) on the Properties of Gray Cast Iron,” J. Inst. Eng. India Ser. D (January-June 2014) Vol. 95 Issue (1), pp. 19-26. DOI 10.1007/s40033-013-0031-3.

[2] Alexander I Krynitsky, Harry Stern “Effect of B in structure and Some Physical Properties of Plain Cast Iron”, Research of National Bureau of Standards, Vol 42 (1949)

[3] Robert Voigt, “ Trace (Minor) Elements in Cast Irons ”, ASM Handbook, Volume 1A, Cast Iron Science and Technology (2017)

[4] S. Pawaskar, L.N. Bartlett, S. Lekakh. 2021, Effect of Boron in Class-30 Gray Iron. AFS Trans. 129, 1-14 (2021).

[5] Maznichevsky, Alexander N., Yuri N. Goikhenberg, and Radii V. Sprikut. “Influence of Nitrogen and Nitride-Forming Elements on Properties of Boron-Treated Steel.” Solid State Phenomena. Trans Tech Publications, Ltd., October 2018. https://doi.org/10.4028/www.scientific.net/ssp.284.621.

[6] J. Sertucha, R. Suárez, J. Izaga, L. A. Hurtado & J. Legazpi (2006) Prediction of solid-state structure based on eutectic and eutectoid transformation parameters in spheroidal graphite irons, International Journal of Cast Metals Research, 19:6, 315-322, DOI: 10.1179/136404606X167114

[7] Doru Michael Stefanescu, Ramon Suarez and Sung Bin Kim, “90 years of thermal analysis as a control tool in the melting of cast iron”, Special review, Vol 17, No 2, (2020)

[8] ASTM International. A48/A48M-03(2016) Standard Specification for Gray Iron Castings. West Conshohocken, PA; ASTM International, 2016. DOI: https://doi-org.libproxy.mst.edu/10.1520/A0048_A0048M-03R16

[9] ASTM International. E10-18 Standard Test Method for Brinell Hardness of Metallic Materials. West Conshohocken, PA; ASTM International, 2018. DOI: https://doi-org.libproxy.mst.edu/10.1520/E0010-18

III. EFFECT OF BORON IN DUCTILE IRON

S. Pawaskar, L.N. Bartlett, S. Lekakh

Department of Material Science and Engineering, Missouri University of Science and Technology, Rolla, MO 65409

Keywords: ductile iron, boron, structure, thermal analysis, mechanical properties

ABSTRACT

Cast iron contamination with boron-containing scraps is becoming a great quality control issue for iron foundries. The effect of boron in ductile is not studied to the extent as to answer the question of the proper mechanism of its effect in ductile iron. Therefore, an experimental study was performed to understand the effects of boron in ductile iron. Ferro-boron additions were used to increase boron up to 150 ppm in laboratory heat. Determination of effects on solidification and eutectoid transformation was done with the help of thermal analysis. Mechanical property tests and microstructural analysis were conducted to determine the effect of boron. The results showed that the boron in ductile iron significantly affected the graphite nodularity and consequently the mechanical properties. Preliminary discussions about the mechanisms of boron effects on phase transformations and properties of ductile iron are presented.

1. INTRODUCTION

Ductile iron (DI) belongs to the family of cast irons with a spheroidal graphite shape. This spheroidal graphite gives DI a higher strength and better ductility than its family counterpart the flake-shaped gray iron. This superiority of DI allows it to be used in multiple mass production applications like pipelines, automotive components, wheels, gearbox, pump housings, and various agricultural equipment applications.

The possibility of steel scrap recycling is an environmental and economic advantage for the cast iron industry. However, with the increased use of boron in automotive steels, B has made its way into the cast iron industry through scraps. Although fresh furnace linings are also a probable source of B in cast iron, the lack of scrap quality control is being considered a problem for the foundries. Although B is considered a residual element, the effects B has on cast iron castings can cause serious quality control issues for foundries.

The effect of B in gray cast iron studied by Alexander [1] suggests that B can be a notoriously strong carbide stabilizer. B was found to increase the carbide levels when added to cast iron with considerable effect on eutectic undercooling. Although this effect can be of positive use in white iron castings by increasing the wear resistance, the increase in carbides can have deleterious effects in gray and ductile irons. As per the data in the Sorel metal handbook [2] for ductile irons, as little as 0.002% B (20ppm) can adversely affect the mechanical properties of the iron. B up to 0.01% can reduce the ductility from 14% to as low as 1% making it brittle. B can also reduce the pearlite stabilizing effect of

elements like Cu and reduce the hardness of castings. Thus, the recommended amount of B in pearlitic irons is also 0.0006% (6ppm)[2].

In another ductile iron study conducted by Mitra [3], B up to 200ppm does not have any considerable effects on ferritic DI pipes performance. It also states that B-added DI pipes tend to have better machinability than the ones without B. These pipes also had a better combination of ductility and hardness than the latter. Similarly, in a technical bulletin published by the Ductile Iron Society [4], ferritic ductile iron castings were unaffected by B addition whereas pearlitic castings showed a decrease in mechanical properties and hardness for B additions as low as 5 to 20ppm. The amount of pearlite forming elements like Cu and Sn were doubled to negate the B effect in these castings. The study also noted that the reduction of B recovered the lost hardness. Reduction of B to 17ppm increased the hardness to 200-210BHN while a further reduction in B up to 6ppm increased the hardness to 230BHN.

Studies conducted by Naro and Wallace [5] also agreed upon the strong carbidic nature of Boron. For a 20ppm addition to a pearlitic ductile iron, the amount of pearlite reduced from 90% to 40% which was accompanied by a complementary rise in ferrite area. But for the second casting with the same 20ppm B addition and identical chemistry, showed no effect on the pearlite fraction rather it increased the hardness values by 10%.

Conclusively, the major effect of B in cast iron is as a strong carbide forming agent. But the effect on the rest of the properties of ductile iron is unclear. Although the effect is higher in pearlitic castings, the mechanism of the effect isn't clearly stated. Along with the mechanism, the studies mentioned above fail to explain a remedy to negate or reduce the effect of B. In one of our previous studies [6], additions of N helped to reduce the effect of

B in class-30 gray cast iron. In the same study, the effect of B is enhanced when Ti was added to the system. The study stated that the effect of B is not just an individual effect but also depends on the amount of N and Ti in the iron. Such a study has not been conducted on ductile iron as of yet.

2. METHODOLOGY

A heat with two different levels of B was performed in a 200lbs coreless induction furnace on the base of technically pure charge materials. The first (base) chemistry was planned to be a 4.2 CE heat with very low B and no B-added. For the second chemistry (B-added), the B was increased to 150ppm with the addition of FeB in the ladle before pouring the molds. Such high B concentration was chosen to verify its effect when a high B contaminated charge could be used. To better observe the potential B-effect on graphite shape, the Mg level was intentionally minimized in the used melt to just above the threshold of producing spherical graphite (<0.04%).

Specifically, the charge for the heats consisted of high purity induction iron ingots, sorel metal (pig iron), ferrosilicon, electrolytic manganese, high purity graphite, ferrosilicon, and foundry returns from our foundry sponsor (Table 1). An argon cover at a flow rate of 25 SCFH was used to increase recovery rates.

CE was checked by thermal analysis and tellurium-added (Te) cup, which was poured after melting all the charge, and before the treatment in the ladle by Mg addition and inoculation. Once CE was confirmed, the melt was tapped in the 200lbs ladle at 1540°C. The 200lbs ladle was modified with a small reaction chamber filled with the Mg-

FeSi and FeSi-based inoculant (Table 1) to improve the Mg recovery and achieve better graphite sphericity. Once the reaction subsided, the chamber was gently removed, and the DI was poured into the molds. For the base-DI, a step block (Figure 1), and three modified keel blocks (ASTM 536 Figure 3 [7]) were poured and a small sample was taken for thermal analysis and chemistry check. After that FeB addition, which was attached to a steel rod, was plunged into the melt, intensively mixed, and the same number of molds were poured from the B-added DI.

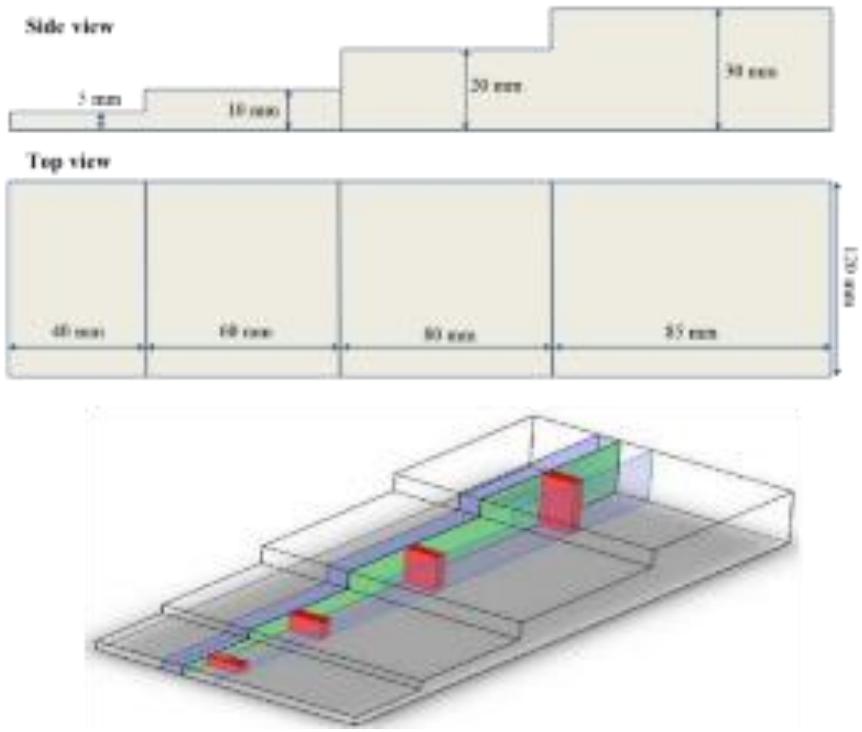

Figure 1. Side, top, and isometric view of step block. The red area was used for metallographic analysis.

Table 1. Chemical composition (wt.%) of the charge materials used for the heat.

Charge Source	C	Si	B	Cr	Mn	Mg	Al	P	S
Waupaca foundry returns	3.47	2.13	0.0004	0.21	0.57	--	--	0.028	0.086
Induction iron	0.0017	0.002	0.0001	0.01	0.01	--	0.002	0.005	0.0025
Sorel metal (pig iron)	4.20	0.15	--	--	0.005	--	--	0.009	--
Ferro-Silicon (Fe75Si)	--	75	--	--	--	--	--	--	--
Ferro-B (Fe18B)	0.26	0.58	18.52	--	--	--	--	0.028	0.003
Desulco graphite	99.99	--	--	--	--	--	--	--	0.008
Electrolytic Manganese	--	--	--	--	100	--	--	--	--
Magnesium Ferro-Silicon	--	44.6				6.13	0.57		
Inoculant	--	71.5	--	--	--	--	4.2	--	--

Thermal analysis and the in-house developed method were used with the help of non-Te cups. The cooling curves analysis was utilized for examining both transformations: liquid/solid and solid/solid eutectoid reaction. The nomenclature of the used solidification parameters is shown in Figure 2 [8].

The chemical composition of the DI was done using Optical Emission Arc Spectroscopy (OES) and C, S, and N from a commercial combustion analyzer from the immersion probe samples. Four standards with 2, 30, 76, and 400ppm B were used for calibration.

Specimens for optical metallography were taken from the step blocks (red sections in Figure 1). For quantifying the metal matrix, etched by 3% Nital images were analyzed using ImageJ software. Tensile samples were prepared with a gauge diameter of 9.07mm and a gauge length of 44.4mm and tested at 0.02mm/s strain rate on a 250kN hydraulic tensile frame in accordance with the ASTM A536 [7]. Hardness tests were performed in accordance with ASTM E10-18 [9] with verification using certified hardness blocks

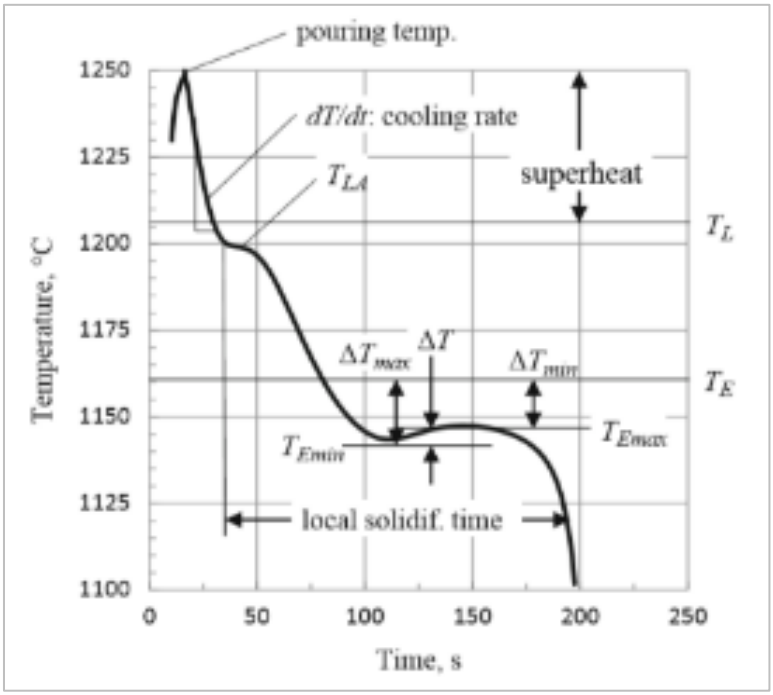

Figure 2. Nomenclature of used parameters for thermal analysis [8].

3. RESULTS

The chemical compositions of the heats obtained from the OES are given in Table 2. The actual chemistries of the heats were close to the target chemistry.

Table 2. Chemical composition for the heat (wt.%).

	C*	Si	CE	B (ppm)	Mg	Mn	Cr	P	S*	N* (ppm)
Base DI	3.45	2.23	4.19	11	0.035	0.23	0.071	0.057	0.010	74
B-added DI	3.51	2.19	4.24	177	0.033	0.23	0.072	0.058	0.013	89

* C, S and N readings taken from commercial C, S, N, O analyzer

3.1. THERMAL ANALYSIS

The solidification cooling curves for both the chemistries are shown in Figure 3. The thermal analysis parameters obtained from thermal analysis software using the non-Te cup are shown in Table 3. Comparing the B-added to base DI, the following changes were observed with B addition: (i) a slight decrease in the liquidus temperature (T_L), (ii) a strong decrease in the temperatures of eutectic reaction start (T_{Emin}, T_{Emax}), and the end of solidification (T_{sol}). Also, GF1, which indicates the changes in graphite precipitated in the semi-liquid stage, increased; GF2 decreased and GF3 which is affected by both, the amount of later precipitated graphite and the graphite nodularity increased.

Table 3. Thermal analysis data obtained from thermal analysis software for both the heats.

Chemistry	Base DI	B-added DI
Liquidus Temp, T_L (˚C)	1169.4	1168.0
Eutectic Start (˚C)	1155.9	1151.0
Eutectic Minimum, T_{Emin} (˚C)	1134.5	1130.0
Eutectic Maximum, T_{Emax} (˚C)	1142.1	1140.3
Solidus Temp (˚C)	1092.5	1089.3
Recalescence, ΔT (˚C)	7.6	10.3
Graphite Factor 1 (GF1)	56	51
Graphite Factor 2 (GF2)	33	31
Graphite Factor 3 (GF3)	63	90

The cooling curves shown in Figure 4 represent the eutectoid reactions for the heat. The 1st derivative of the cooling curve was plotted against the temperature for the eutectic

and eutectoid reactions to analyze the change in cooling rates related to the latent heat liberation. These results are presented in the discussion part of this article.

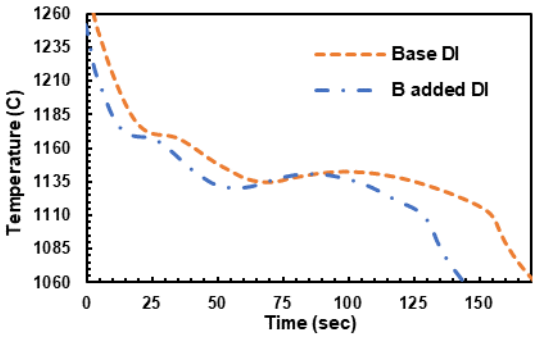

Figure 3. Solidification cooling curve for both the DI.

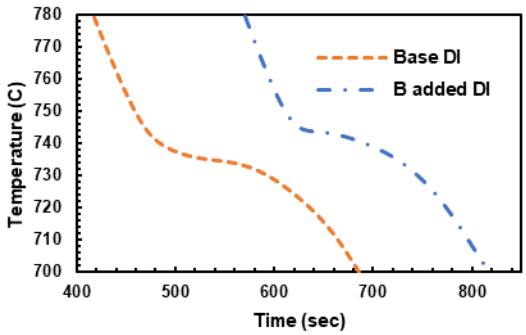

Figure 4. Eutectoid cooling curve for both the DI.

3.2. MICROSTRUCTURE

The unetched microstructures obtained from the step block for the base and the B-added chemistries are shown in Figure 5 and Figure 6 respectively. The graphite sphericity is clearly higher in the base DI irrespective of the step-block thickness. However, with the

addition of B, the sphericity of the graphite is affected heavily by the cooling rate. At a low cooling rate, the shape of graphite in the B-added specimens looks like an exploded graphite. The etched microstructures obtained from the step block for the base and the B-added chemistries are shown in Figure 7 and Figure 8 respectively. In the base DI, the bull's-eye pattern associated with ductile iron is seen with the matrix being primarily pearlitic, however, some carbide precipitation was seen in the 5mm step. In the B-added DI, carbide precipitation was observed in all the steps irrespective of thickness.

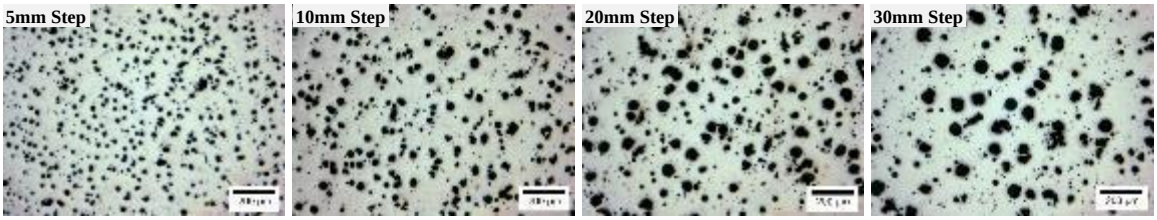

Figure 5. Unetched microstructures taken from the step block of the base DI (increasing thickness L-R).

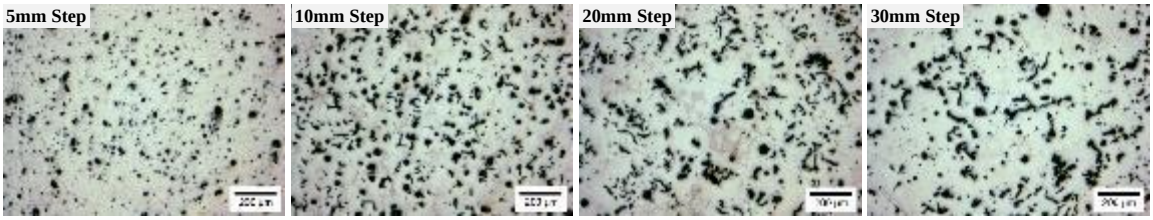

Figure 6. Unetched microstructures taken from the step block of the B-added DI (increasing thickness L-R)

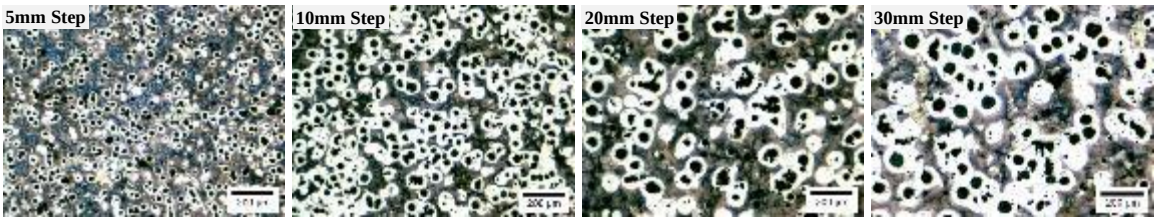

Figure 7. Etched microstructures taken from the step block of the base DI (increasing thickness L-R).

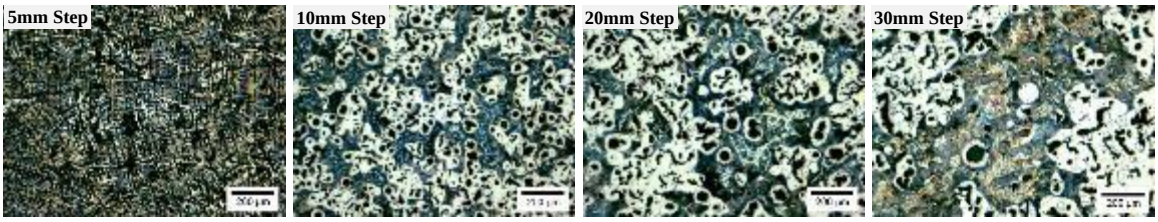

Figure 8. Etched microstructures taken from the step block of the B-added DI (increasing thickness L-R).

3.3. MECHANICAL PROPERTIES

The mechanical properties of this heat are presented in the Table. 4. It is seen that the mechanical properties degrade significantly with the addition of B. The ultimate tensile stress drops, and the ductility is reduced to half. The results are plotted graphically as shown in Figure 9. The yield stress of the specimens was calculated as shown in Figure 10 by selecting a line of best fit for the linear region of the tensile curves and translating the line to a 0.2% yield offset. The yield stress results do not show any considerable variation. Also, the hardness which was calculated on the tensile bar specimens did not show any major variations either.

Table 4. Mechanical properties for the heat.

Chemistry	Base DI	B-added DI
Ultimate Tensile Strength (MPa)	531 ± 22	513 ± 28
0.2 Yield Strength (MPa)	343 ± 17	344 ± 21
Elongation (%)	9.3 ± 0.7	5.4 ± 0.5
Hardness (BHN)	184 ± 1	183 ± 1

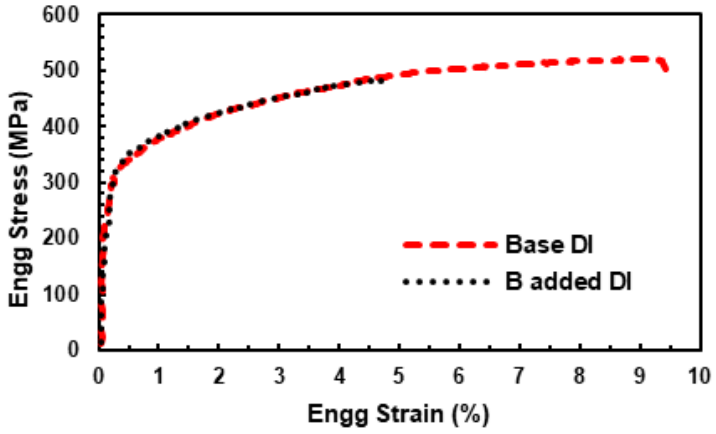

Figure 9. Comparison of tensile test curves for the two chemistries.

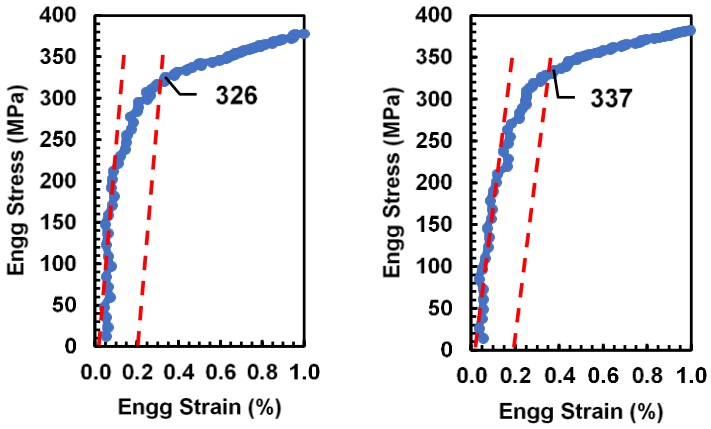

(a) (b)

Figure 10. Calculation of 0.2 offset yield strength for (a) Base DI and (b) B-added DI.

4. DISCUSSION

4.1. SOLIDIFICATION

Presented data from thermal analysis and microstructure indicated that the studied B addition had a significant effect on solidification. To exclude the possible differences in solidification time and its effects, cooling curves were plotted in coordinates of the first temperature derivative vs temperature (Figure 11). B caused a slight decrease in the liquidus temperature. This is the exact opposite of the effect observed in our gray iron study[10]. Such comparison indicates a possible mutual B and Mg interaction in the because both B and Mg could potentially form carbides.

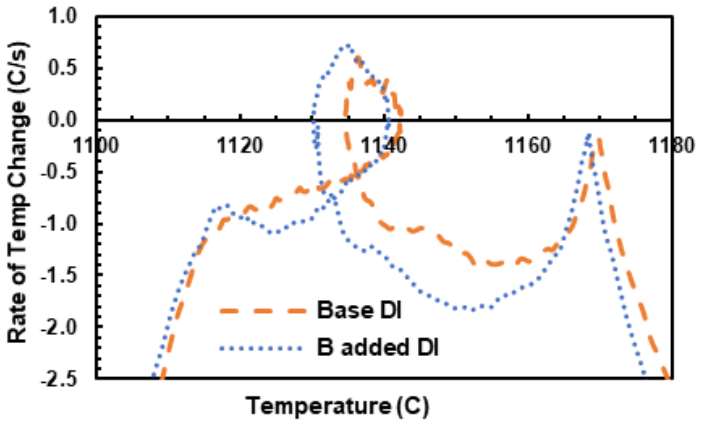

Figure 11. 1st derivative of the cooling curve in the solidification region plotted against temperature for both the chemistries.

Along with the liquidus (T_L), B also strongly affected the eutectic solidification including the graphite nucleation and growth processes. The reduction of eutectic start

temperature with the addition of B suggests that the graphite nucleation is affected adversely. Such a significant reduction in the eutectic low temperature (T_{EMin}) indicates a higher tendency of carbide precipitations in the B-added chemistry, which were detected in the step block. These effects are observable in Figure 11. The peaks on the right symbolize the liquidus temperature (T_L). For the eutectic parameters, the left side of the loop is the eutectic low temperature (T_{EMin}) whereas the right side of the loop is eutectic high (T_{EMax}). The loop diameter gives us the eutectic recalescence. The graph indicates that the addition of B shifted eutectic solidification to a lower temperature window. First derivative values are related to the latent heat released and it could be affected by two other factors simultaneously: the amount of eutectic phases precipitated and their latent heat of formation. C precipitation in graphite provides larger specific latent heat when compared to cementite.

On the other side, the cementite growth, without C being enveloped in austenite as graphite nodules, is much faster because it is less dependent on C diffusion. The base DI with perfect spherical graphite nodules did not show high recalescence which in comparison to B-added DI, vermicular shape nodule graphite had a faster growth with some direct contact with the remained melt. Such changes in phase composition and phase shape will affect the recalescence. Also, changes in GF1 indicated a decrease in graphite precipitated in the semi-liquid stage and there was a decrease in GF2 which is the angle of the derivative just before the solidus, which is affected by many factors including, the amount of later precipitated graphite and the graphite nodularity.

4.2. EUTECTOID TRANSFORMATION

Because the changes in the eutectoid parameters for both ductile irons were not visible directly from the cooling curve (Figure 4), the derivative thermal analysis was performed (Figure 12). The occurring solid-state transformation is also accompanied by a release of latent heat resulting from the formation of ferrite and pearlite phases from decomposed austenite. Sertucha et.al [11] showed that two parameters V_{Trans} and T_{Trans} can be used to analyze solid-state transformations, where V_{Trans} is the maximum value of the 1st derivative of temperature and T_{Trans} is the temperature associated with the highest value of V_{Trans}. There are no recalescence loops formed in the graph for both DI, which can be interpreted as no positive V_{Trans} values. In general, a positive value of V_{Trans} is an indication that the latent heat released from the solid-state transformation is high enough to overcome the temperature drop associated with the sample cooling down. Ferrite transformations occur at a higher temperature than pearlite, as the decomposition of austenite to lamellar pearlite (carbide + ferrite) requires a lower temperature i.e., an increased eutectoid undercooling. From the graph, it can be seen that the B-added DI can have a higher ferrite forming tendency as compared to the base-DI. This can also be attributed to the fact that the graphite shape for the B-added specimen is an exploded graphite which is in close proximity to each other. This proximity can result in facilitating the movement of C from the austenite matrix to the graphite (acting as a C sink), thus depleting the matrix of C and forming ferrite.

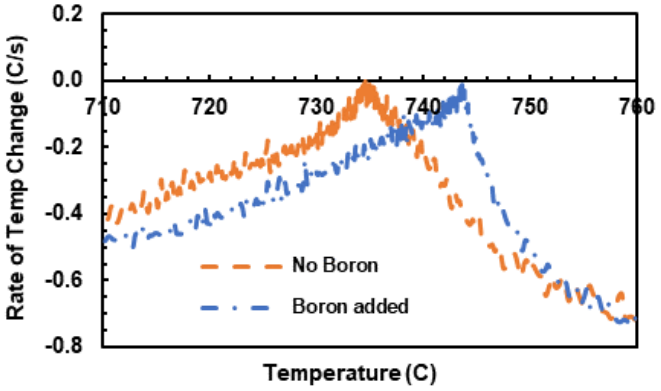

Figure 12. 1st derivative of the cooling curve during the eutectoid reaction plotted against temperature for both the chemistries. The peak in the graph is the V_{Trans} and the temperature corresponding to it is T_{Trans}

4.3. MICROSTRUCTURE AND MECHANICAL PROPERTIES

On analyzing the microstructures shown in Figure 5 and Figure 6, it can be seen that the addition of B can severely affect the sphericity of graphite nodules making them into exploded graphite and the high cooling rate in the thin step did not recover spherical shape. On analyzing the etched samples from Figure 7 and Figure 8, the B-added specimen has considerable carbide precipitation. The matrix for the base DI is pearlitic with ferrite surrounding the graphite nodules and carbide precipitation only in the 5 mm step. For the B-added DI, the carbide precipitation occurred even in the 30mm step. Generally, the formation of carbides occurs due to a high cooling rate and/or a low graphite nucleation potential. In our previous gray iron study[10], B supported the graphite nucleation by increasing the eutectic start temperature. However, it is the exact opposite for ductile iron. This means that B can act as an inhibitor to Mg action in ductile iron and the details of the mechanism needed to be verified in the future.

When compared with the base DI, the mechanical properties of B-added specimens are undesirable because the loss in ultimate tensile strength and maximum elongation was significant. The ductility of ductile iron is reduced to as much as 50% with the addition of B. This loss in ductility and strength can be attributed to the graphite shape. The sphericity of graphite in ductile iron is crucial for its mechanical properties. The nodular graphite reduces the risk of crack initiation and resists crack propagation when compared with the flake graphite of cast iron. The exploded graphite in the B-added specimens can become an initiation site for a crack.

5. CONCLUSION

The effects of B on ductile iron were studied on a heat designed with a technically pure charge material (base-DI) and B-added chemistry. The effect of B on solidification was studied using thermal analysis. The effect of B on austenite in ductile iron is opposite of what is seen in cast iron as it reduces the stability of austenite by reducing the liquidus temperature. The eutectic parameters are adversely affected with the addition of B as the eutectic temperatures dropped, which is strong proof that B has very strong carbide stabilizing properties. The reduction in eutectic start temperature indicates that B can also interfere with the nucleation potential of graphite. During the solid-state transformation, B can result in a higher solid-state transition temperature T_{Trans}, resulting in higher ferrite content in the matrix. This however is more due to the irregular shape of graphite seen from the microstructure analysis. B can severely affect the sphericity of graphite nodules making them into exploded graphite. This exploded graphite can result in graphite being close to

each other thus facilitating the transfer of C from austenite to graphite and consequently increasing the ferrite content in the matrix. The precipitation of carbide in the etched microstructures of the step block further cements the strong carbide stabilizing properties of B. The mechanical properties of ductile iron are also affected adversely due to the addition of B. The reduction in strength and ductility are detrimental to ductile iron properties which are caused due to irregular graphite shapes in the B-added specimen. To conclude, the effect of B in ductile is more severe than that in gray iron with flake graphite, due to its interference with the spheroidizing properties of Mg.

ACKNOWLEDGEMENT

This investigation was funded by the American Foundry Society. The authors would like to thank the Foundry partners and the Cast-Iron research committee for their continued support and guidance throughout this project. The authors would like to acknowledge the contributions of the Graduate and Undergraduate research students and staff at Missouri S&T for their assistance at every step of this project.

REFERENCES

[1] Alexander I Krynitsky, Harry Stern “Effect of B in structure and Some Physical Properties of Plain Cast Iron”, Research of National Bureau of Standards, Vol 42 (1949)

[2] Rio Tinto Iron and Titanium Inc. 2004. The Sorelmetal Handbook of Ductile Iron. Montreal, Quebec: Rio Tinto Iron and Titanium Inc.

[3] Mitra, Subhajit, Debdas Roy, Tanmay Bhattacharyya, and P P Chattopadhyay. 2018. "Effect of boron on the manufacturing process and final properties of ductile iron pipes (DI pipes)." Ironmaking and Steelmaking 45: 1-5. DOI:10.1080/03019233.2017.1286546.

[4] Gundlach, Richard. 2003. "The Effect of Boron in Ductile Iron." Hot Topics. The Ductile Iron Society.

[5] Naro, R L, J F Wallace, and Yulong Zhu. 2003. "Elimination and Neutralization of Boron in Ductile Irons." DIS Project. August.

[6] S. Pawaskar, L.N. Bartlett, S. Lekakh. 2021, Effect of Boron in Class-30 Gray Iron. AFS Trans. 129, 1-14 (2021).

[7] ASTM International. A536-84(2019)e1 Standard Specification for Ductile Iron Castings. West Conshohocken, PA; ASTM International, 2019. DOI: https://doi.org/10.1520/A0536-84R19E01

[8] Doru Michael Stefanescu, Ramon Suarez and Sung Bin Kim, “90 years of thermal analysis as a control tool in the melting of cast iron”, Special review, Vol 17, No 2, (2020)

[9] ASTM International. E10-18 Standard Test Method for Brinell Hardness of Metallic Materials. West Conshohocken, PA; ASTM International, 2018. DOI: https://doi-org.libproxy.mst.edu/10.1520/E0010-18

[10] J. Sertucha, R. Suárez, J. Izaga, L. A. Hurtado & J. Legazpi (2006) Prediction of solid-state structure based on eutectic and eutectoid transformation parameters in spheroidal graphite irons, International Journal of Cast Metals Research, 19:6, 315-322, DOI: 10.1179/136404606X167114

[11] S. Pawaskar, L.N. Bartlett, S. Lekakh. 2022, Mutual B, Ti, N effects on phase transformations in cast iron: Thermodynamic consideration and experimental verification. AFS Trans. 130, 1-11 (2022).

SECTION

3. CONCLUSION

The effect of boron on gray cast iron properties like microstructure, mechanical properties, and solidification was successfully studied. Thermal analysis conducted on Class-30 gray iron highlighted the effect boron has on the austenite stability. The proportional increase in liquidus of the iron with boron content was clearly shown and resulted in increased stability of austenite. Along with stabilizing austenite, boron also was found to be a carbide stabilizing element as it increased the eutectic undercooling. The use of chill wedges also highlighted the carbide forming abilities of boron. Considering the eutectoid reactions, the ferrite stabilizing property of boron was revealed. The use of derivative thermal analysis gave concrete proof that increasing boron can lead to an increase in ferrite area fraction in the casting which can cause reduced hardness and strength. The microstructure analysis of the step block castings poured from various heats confirmed these findings as there was an increase in the area fraction of ferrite with increasing boron content. Although these results were consistent with different levels of carbon and silicon, the intensity of the effects varied. This can be an indication that the effect of boron may also be dependent on the carbon equivalent. These results were in agreement with the available literature, which stated that the effect of boron on ferritic ductile irons was not as evident as it was on the pearlitic ductile iron with lower carbon equivalents.

In the second part of this study, the effect of boron in conjunction with elements like nitrogen, titanium, and tin was studied with the help of thermodynamic simulations and validated by performing experimental heats. The use of thermodynamic software led to the development of a new concept to understand the mechanism of boron in cast iron, the concept of ‘free Boron’. This concept assumes that the Boron, which is not tied up as boron nitrides can affect the properties of cast iron. The hypothesis was simulated for different compositions of boron, and it also predicted the mutual effects of other purities in cast iron. The simulations demonstrated that increasing the amount of nitrogen in the melt can tie up boron and prevent “free boron” in solution from interacting with carbon diffusion. It also showed that titanium can enhance the effectiveness of boron by decreasing the amount of nitrogen in solid solution and increasing ‘free Boron’. The hypothesis and concept of ‘free Boron’ were verified by the experimental heat.

In the third part of this study, the effect of boron in ductile iron was studied on ductile iron by designing a casting trial of base chemistry ductile iron and with additions of boron. The use of thermal analysis helped uncover the effect of boron during ductile iron solidification and solid-state transformations. The addition of boron adversely affected the austenite stability, decreased the graphite eutectic temperature, and resulted in a compacted graphite shape. Boron also increased the carbide precipitation in the iron. The severe effect of boron on graphite sphericity was observed from microstructure analysis, which also resulted in a 50% drop in the total elongation.

The effect of boron cannot just be considered as an individual effect. The intensity of the boron effect is higher at a lower CE than at a higher CE, which indicates that boron can be a bigger problem for pearlitic castings than ferritic castings. Majorly, boron acts as

a strong carbide stabilizer and a ferrite promoter in gray iron. Despite the increase in ferrite, the strength of boron -added gray iron may increase which might be due to the increase in carbides or precipitation of BN within the ferrite. Whereas in ductile iron, boron can have severe effects on the graphite sphericity and also results in significant carbide formations even in thick castings and deterioration of mechanical properties. In order to determine the effectiveness of boron in the iron, impurities like N and Ti also have to be considered. N can help prevent the detrimental effects of boron, but for the same level of boron, even 0.05% levels of Ti can result in an augmented effect of boron at stabilizing ferrite. Considering the data from the thermodynamic simulations, to tie up 30ppm of boron, at least 50ppm N is required and if Ti is at a level of 0.05%, the required N can increase up to 70ppm and even higher for higher levels of Ti. Therefore, the safe limit of boron in cast iron depends on the allowable N in the system.

4. FUTURE WORK

With the help of thermal analysis and microstructure analysis, the effect of Boron was studied and mechanisms for these effects were predicted precisely. However, since the actual distribution of Boron in the cast iron phases was not studied, these predicted mechanisms could not be verified completely. For future work, the analysis of Boron in the matrix and its actual distribution in the matrix is required. Given the small atomic number of Boron, the use of SEM/TEM or Wavelength Dispersive Spectroscopy can be a viable option for the analysis. However, the major difficulty in these kinds of analyses can be the Boron concentration in the specimens. Since the critical Boron in these studies are at the order of 100-150ppm, it can affect the results of Energy dispersive spectroscopy because the threshold concentration of these methods is a minimum of 0.5 – 1.0% (500 to 1000ppm). Although there can be an option of doping the specimen with higher amounts of Boron (up to 1%) just to understand the segregation tendencies of Boron, these concentrations of Boron will not be much for industrial and practical usage.

Another prospect for this study can be studying the effect of Boron on graphite structure and shape. Given the effect of Boron on eutectic parameters in gray iron, analysis of graphite shape and size with parameters like maximum flake thickness, length, graphite particle count and area fraction can help characterize the effect Boron has on these properties. The use of ImageJ and using the Analyze particle feature can help understand some of the above-mentioned parameters, the results from ImageJ are restricted by the minimum pixel size and the image taken. The use of automated SEM scanning for graphite analysis can help overcome the drawbacks of ImageJ analysis. With the feature of

automated scanning, the entire specimen (which is only restricted by the size of the sample holder) can be scanned. This scanning can give the maximum thickness of the flake, and flake area fraction. The challenge this method can face is the non-linear shape of the graphite flakes, which can result in the improper measurement of the maximum length of the flake.

For studies involving ductile iron, chemistries with different carbon equivalents can be analyzed to measure if the effect of Boron is dependent on carbon equivalent as seen in the gray iron study. Also, the mutual effect of Boron with Magnesium can be studied by performing more iterations with varying Boron and Magnesium levels to determine the exact relationship of the Boron effect with the amount of Magnesium in ductile iron.

BIBLIOGRAPHY

[1] Goodrich, George M. 2008. *Introduction to Cast irons.* Vol. 1A Cast Iron Science and Technology, in *ASM Handbook*, edited by Diran Apelian, Raymond J. Donahue, Babu DasGupta, Michael Gywn, John L. Jorstad, Raymond W. Monroe, Mahi Sahoo, Thomas E. Prucha, Daniel Twarog Srinath Viswanathan, 785-811. ASM International. doi:10.31399/asm.hb.v15.a0005322.

[2] Stefanescu, Doru M. 2017. *Classification and Basic Types of Cast Iron.* Vol. 1A Cast Iron Science and Technology, in *ASM Handbook*, edited by Doru M. Stefanescu, 12-27. ASM International. doi:10.31399/asm.hb.v01a.a0006294.

[3] Stefanescu, Doru M., Katz, Seymour. 2008. *Thermodynamic Properties of Iron-Base Alloys.* Vol. 15 Casting, in *ASM Handbook*, edited by Diran Apelian, Raymond J. Donahue, Babu DasGupta, Michael Gywn, John L. Jorstad, Raymond W. Monroe, Mahi Sahoo, Thomas E. Prucha, Daniel Twarog Srinath Viswanathan, 41-55. ASM International. doi:10.31399/asm.hb.v15.a0005190.

[4] 2008. *Gray Iron Castings.* Vol. 15 Casting, in *ASM Handbook*, edited by Diran Apelian, Raymond J. Donahue, Babu DasGupta, Michael Gywn, John L. Jorstad, Raymond W. Monroe, Mahi Sahoo, Thomas E. Prucha, Daniel Twarog Srinath Viswanathan, 835-855. ASM International. doi:10.31399/asm.hb.v15.a0005323.

[5] Goodrich, George M. 2008. *Ductile Iron Castings.* Vol. 15 Casting, in *ASM Handbook*, edited by Diran Apelian, Raymond J. Donahue, Babu DasGupta, Michael Gywn, John L. Jorstad, Raymond W. Monroe, Mahi Sahoo, Thomas E. Prucha, Daniel Twarog Srinath Viswanathan, 856-871. ASM International. doi:10.31399/asm.hb.v15.a0005324.

[6] 2008. *Compacted Graphite Iron Castings.* Vol. 15 Casting, in *ASM Handbook*, edited by Diran Apelian, Raymond J. Donahue, Babu DasGupta, Michael Gywn, John L. Jorstad, Raymond W. Monroe, Mahi Sahoo, Thomas E. Prucha, Daniel Twarog Srinath Viswanathan, 872-883. ASM International. doi:10.31399/asm.hb.v15.a0005325.

[7] Gundlach, Richard B. 2008. *White Iron and High-Alloyed Iron Castings.* Vol. 15 Casting, in *ASM Handbook*, edited by Diran Apelian, Raymond J. Donahue, Babu DasGupta, Michael Gywn, John L. Jorstad, Raymond W. Monroe, Mahi Sahoo, Thomas E. Prucha, Daniel Twarog Srinath Viswanathan, 896-903. ASM International. doi:10.31399/asm.hb.v15.a0005327.

[8] van Ettinger, C.J. 2008. *Malleable Iron Castings.* Vol. 15 Casting, in *ASM Handbook*, edited by Diran Apelian, Raymond J. Donahue, Babu DasGupta, Michael Gywn, John L. Jorstad, Raymond W. Monroe, Mahi Sahoo, Thomas E. Prucha, Daniel Twarog Srinath Viswanathan, 884-895. ASM International. doi:10.31399/asm.hb.v15.a0005326.

[9] Atlan, Taylan. 2007. "R&D Update: Hot-stamping boron-alloyed steels for automotive parts - Part I." *Stamping Journal*, Feb 13. https://www.thefabricator.com/stampingjournal/article/stamping/hot-stamping-boron-alloyed-steels-for-automotive-parts.

[10] Ankamma, Kandula. 2014. "Effect of Trace Elements (Boron and Lead) on the Properties of Gray Cast Iron." *Journal of The Institution of Engineers (India): Series D* 95 (1): 19-26. doi:10.1007/s40033-013-0031-3.

[11] El-Shennawy, M. 2016. "Effect of Boron content on Metallurgical and Mechanical Characteristics of Low Carbon Steels." *International Journal of Mechanical Engineering (IJME)* 1-14.

[12] Schwartz, H. A. 1944. "Boron as an accelerator of Malleable Annealing." *Technical Data Digest*, September: 45.

[13] Bastien, P. G., and L Guillet Jr. 1938. *The Influence of some special additions on certain properties of cast iron.* Vol. 27, in *Carnegie Scholarship Memoirs*, by Iron and Steel Institute, edited by George C. Lloyd, 77. California: E. & F. N. Spon, Limited.

[14] ASTM International. *A247-19 Standard Test Method for Evaluating the Microstructure of Graphite in Iron Castings*. West Conshohocken, PA; ASTM International, 2019. doi: https://doi-org.libproxy.mst.edu/10.1520/A0247-19

[15] Krynitsky, Alexander I. 1949. "Effect of Boron on the structure and some physical properties of plain Cast Irons." *Journal of Research of the National Bureau of Standards* (U.S Department of Commerce National Bureau of Standards) 42: 465-479.

[16] Eckman, Harry A, and Henry W Maack. 1951. Malleable Iron with Boron and Bismuth. Ed. United States Patent Office. Chicago, United States Patent 2,579,452. December 25.

[17] Bedolla-Jacuinde, A., F.V. Guerra, A.J. Guerrero-Pastran, M.A. Sierra-Cetina, and S. Valdez-Medina. 2021. "Microstructural effect and wear performance of high chromium white cast iron modified with high boron contents." *23rd International Conference on Wear of Materials.*

[18] Rio Tinto Iron and Titanium Inc. 2004. *The Sorelmetal Handbook of Ductile Iron.* Montreal, Quebec: Rio Tinto Iron and Titanium Inc.

[19] Mitra, Subhajit, Debdas Roy, Tanmay Bhattacharyya, and P P Chattopadhyay. 2018. "Effect of boron on the manufacturing process and final properties of ductile iron pipes (DI pipes)." *Ironmaking and Steelmaking* 45: 1-5. doi:10.1080/03019233.2017.1286546.

[20] Strande, Knud, Niels Skat Tiedje, and Ming Chen. 2017. "A Contribution to the Understanding of the Combined Effect of Nitrogen and Boron in Grey Cast Iron." Edited by Thomas Prucha. *International Journal of Metalcasting* 11: 61-70. doi:https://doi.org/10.1007/s40962-016-0079-6.

[21] Eppich, Robert. 2005. Cast Iron alloy containing Boron. Ohio, USA Patent WO 2006/133355 A2. June 8.

[22] Naro, R L, J F Wallace, and Yulong Zhu. 2003. "Elimination and Neutralization of Boron in Ductile Irons." *DIS Project.* August.

[23] Gundlach, Richard. 2003. "The Effect of Boron in Ductile Iron." Hot Topics. The Ductile Iron Society.

VITA

Suyash Surendra Pawaskar was born in Rasayani, near Panvel in Maharashtra, India. He finished his Bachelor's in Engineering from Pillai HOC College of Engineering and Technology, Rasayani in the year 2016. After finishing his Bachelors, he worked as Quality Control Mechanical tester trainee in POSCO Maharashtra, Mangaon, India from Aug 2016 to Dec 2016. After completing his training period, he was transferred to the Quality Control where he worked as a Quality Control Executive for the same industry. With the primary responsibility of handling Galvanized and Galvannealed rolled product customers, he worked there till Oct 2018. He then decided to pursue his master's degree in the US in Metallurgical Engineering.

He joined Missouri University of Science and Technology, Rolla MO in Aug 2019. He started as a Graduate Research Assistant under Dr. Laura Bartlett and Dr. Simon Lekakh with the research topic of understanding the effects of Boron in cast iron. During his program, he studied the effect Boron causes on the various aspects of cast iron like solidification, solid-state transformations, microstructure, and mechanical properties. He also published two conference proceedings and one journal article on the research he conducted. Suyash received his master's in science degree in Metallurgical Engineering from Missouri University of Science and Technology in July 2022.